https://doi.org/10.5194/egusphere-2026-2982
Preprint. Discussion started: 19 June 2026

Impacts of All-Sky Himawari-9 AHI Radiance Assimilation on Cloud and Precipitation Forecasting over the Maritime Continent (JEDI-MPAS 3.0.3)

Xuewei Zhang,[1,3] Zhiquan Liu[1], Lipeng Jiang,[1,4], Tao Sun[2], I-Han Chen[2], Dale M. Barker[2], Jinzhong Min[3]

[1]NSF National Center for Atmospheric Research, Boulder, Colorado, USA
[2]Centre for Climate Research Singapore, Singapore
[3]Key Laboratory of Meteorological Disaster, Ministry of Education (KLME)/Joint International Research Laboratory of Climate and Environment Change (ILCEC)/Collaborative Innovation Center on Forecast and Evaluation of Meteorological Disasters (CIC-FEMD), Nanjing University of Information Science & Technology, Nanjing, China
[4]Earth System Modeling and Prediction Center, China Meteorological Administration, Beijing, China

Correspondence to: Zhiquan Liu (liuz@ucar.edu)

Abstract. The Maritime Continent remains a long-standing challenge for numerical weather prediction (NWP). Accurate prediction of tropical convection over this region is further complicated by its small spatial scales, rapid evolution, and strong nonlinearity. Geostationary infrared (IR) satellite observations are widely regarded as one of the most valuable data sources for regional NWP by offering high temporal and spatial resolution over a broad domain. This capability enables near-continuous monitoring of rapidly evolving weather systems from mesoscale to convective scale. Therefore, this study investigates the impacts of all-sky IR radiance assimilation on cloud and precipitation forecasts over this area. Both water vapor channels 8-10 and the cloud-sensitive window channel 13 from the new-generation Himawari-9 Advanced Himawari Imager (AHI) are assimilated using hybrid 3D/4DEnVar methods within the MPAS-JEDI system. Cycling assimilation experiments are conducted to systematically evaluate their impacts on the analysis, background, and forecast fields using multiple independent observations. Results suggest that, relative to clear-sky assimilation, the analyses of brightness temperatures and cloud-top heights from the all-sky AHI assimilation experiments exhibit a better fit to the all-sky observations. Background verification indicates overall neutral-to-positive impacts, with particularly pronounced improvements in humidity. Furthermore, short-range cloud and precipitation forecast errors are generally reduced in the AHI assimilation experiments. Adding channel 13 further enhances rainfall forecast skill during the first 12 hours, whereas the 4DEnVar framework yields more sustained improvements at longer lead times. These results underscore the promise of all-sky AHI radiance assimilation for improving convection-permitting forecasts over the Maritime Continent.

https://doi.org/10.5194/egusphere-2026-2982
Preprint. Discussion started: 19 June 2026

1 Introduction

The Maritime Continent remains one of the most challenging regions for numerical weather prediction (NWP), owing to its irregular land – sea distribution, strong ocean – atmosphere coupling, complex multiscale interactions, and sparse in situ observations (Medeiros et al., 2021; Gehne et al., 2022; Stephens et al., 2024). Under such conditions, the prediction of tropical convective systems is further complicated by their small spatial scales, rapid development, and inherent nonlinearity. Despite substantial advances in NWP models, including convection-permitting resolutions, improved dynamical cores, and more sophisticated physical parameterizations (Rao et al., 2023; Matsunobu et al., 2024), forecast accuracy remains highly dependent on the quality of the initial conditions (Johnson and Wang, 2024; Gao et al., 2026). Accordingly, increasing efforts have been devoted to the assimilation of high-resolution observations to better constrain the initial atmospheric state, thereby enhancing subsequent forecasts of cloud, precipitation and associated high-impact weather (Hu et al., 2023).

Geostationary infrared (IR) satellite observations are widely regarded as one of the most valuable data sources for regional NWP because of their high temporal and spatial resolution over a broad, fixed domain. This unique capability allows near-continuous monitoring of rapidly evolving weather systems across scales from α/β-mesoscale to convective scale. Early efforts to assimilate these high-resolution data were largely limited to the clear-sky IR radiances, which have been shown to improve the thermal and moisture structure of the model initial state (Zou et al., 2015; Yang et al. 2017; Hutt et al., 2020). Nonetheless, a large proportion of satellite observations in cloudy scenes are excluded when using clear-sky assimilation approach, thereby limiting data utilization. This limitation is likely to be further amplified in tropical regions, where deep convective cloud systems occur frequently (Ruppert et al., 2020). Moreover, the cloud-detection process used in clear-sky data assimilation may introduce sampling errors when separating clear-sky from cloudy scenes, thereby degrading analysis quality (Stengel et al., 2013). These factors led to growing interest in the all-sky assimilation of geostationary IR observations from sensors such as AHI, ABI, and AGRI for regional forecasting (Zhang et al., 2016; Honda et al., 2018; Geer et al., 2019). However, extending their use to cloudy scenes remains more challenging than clear-sky assimilation. These challenges are associated with strong nonlinear relationships among radiances, cloud fraction, and cloud-top height, the non-Gaussianity statistics, and imperfect representations of cloud-related processes in both NWP models and radiative transfer operators, all of which may degrade assimilation performance (Chan et al., 2020; Li et al., 2022). Nevertheless, a few studies have demonstrated the promise of all-sky IR radiance assimilation, as discussed below.

Among geostationary IR imagers, the Himawari-8 Advanced Himawari Imager (AHI), operated by the Japan Meteorological Agency (JMA), has been widely employed in data assimilation because of the high-quality of its observations and its potential value to improve weather prediction. For example, it was found that assimilating Himawari-8 AHI channel 9 radiances at 10 min intervals using a local ensemble transform Kalman filter could improve the analysis of tropical cyclone structure and moisture transport, which in turn led to more accurate forecasts of the September 2015 Kanto–Tohoku heavy rainfall event (Honda et al., 2018). Extending this effort to a convection-permitting model with a finer 2 km grid spacing, Sawada et al. (2019) applied a similar rapid-cycling strategy to assimilate all-sky Himawari-8 AHI band 8 (6.2 μm) and band

https://doi.org/10.5194/egusphere-2026-2982
Preprint. Discussion started: 19 June 2026

10 (7.3 µm) water vapor radiances, resulting in improved analyses and forecasts of isolated convective cells and localized severe rainfall. To further reduce the computational cost of all-sky AHI radiance assimilation, Wang et al. (2022) implemented a dual-resolution hybrid EnVar scheme for Himawari-8 AHI water vapor bands 8-10. Despite the lower cost, this configuration was shown to retain forecast skill comparable to that of the full-resolution hybrid EnVar while producing generally positive impacts on rainfall forecasts, particularly at higher precipitation thresholds.

Comparable progress has also been reported for the National Oceanic and Atmospheric Administration's GOES series, particularly for the Advanced Baseline Imager (ABI) aboard GOES-16. Based on the convection-permitting Warn-on-Forecast system, the assimilation of GOES-16 ABI water vapor channels together with cloud water path retrievals was shown to improve the prediction of convective initiation (Jones et al., 2020). However, an upper-level cloud bias was also noted, characterized by an overestimation of cloud optical thickness, which might be attributed to deficiencies in representing the optical properties of thin cirrus in the fast radiative transfer model and to uncertainties in the nonlinear relationship between hydrometeors and radiances. More recently, Degelia et al. (2023) developed an RRFS-based EnVar approach in which brightness temperature (BT) was directly used as a control variable for the assimilation of GOES-16 ABI all-sky channel 10 radiances, thereby alleviating gradient imbalance, suppressing spurious convection, and improving forecasts of localized convective events. In terms of tropical cyclone prediction, more accurate track and intensity forecasts for Laura (2020) and Ida (2021) were achieved through the all-sky assimilation of ABI channel 10, combined with the clear-sky assimilation of the remaining water vapor channels (Feng and Pu, 2025).

With respect to China's Fengyun-4A Advanced Geostationary Radiation Imager (FY-4A AGRI), previous studies have likewise demonstrated the potential benefits of all-sky IR radiance assimilation for improving short-range forecasts of mesoscale weather systems, including heavy rainfall and typhoons. Moreover, the impact of all-sky IR data assimilation has also been examined in tropical convective environments over data-sparse oceanic regions. For instance, within a 9 km WRF-EnKF framework, the assimilation of the Meteosat-7 6.4 µm water vapor channel was shown to improve the representation of cloud patterns at spatial scales exceeding 100 km, as verified against independent 11.5 µm window channel observations from Meteosat-7 (Chan et al., 2020). Beyond IR water vapor channels, recent studies have also suggested that visible and near-IR observations enable more direct fine-scale constraints on cloud and convective structures, with corresponding benefits for cloud and precipitation forecasts (Scheck et al., 2020; Xie et al., 2025; Kugler and Weissmann, 2025). However, their utility is inherently limited to daytime conditions and surface effects, with the associated benefits becoming more evident when these observations are assimilated jointly with IR channels.

Despite these advances, studies on the all-sky assimilation of geostationary IR window channel radiances remain relatively limited. Furthermore, most previous studies have focused on severe weather systems in midlatitude regions, while the potential value of all-sky IR radiance assimilation for tropical weather has not yet been fully explored. Convective systems associated with clouds and precipitation over the tropics often exhibit greater spatiotemporal variability and less coherent organization, which may pose additional challenges for data assimilation. In this context, this study presents the first attempt to assimilate newly available all-sky radiance observations from Himawari-9 AHI, with both water vapor and window channels jointly assimilated using a three-/four-dimensional (3D/4D) hybrid EnVar framework in the MPAS-JEDI system. This study further investigates how all-sky radiance assimilation affects the analysis and short-range prediction of tropical clouds and precipitation over the Maritime Continent, with the aim of improving the effective use of AHI IR observations under cloudy conditions.

The paper is organized as follows. In section 2, an overview of the methodology is provided, including an introduction of the observations and their preprocessing, the observation-error modelling schemes, and the data assimilation system adopted in this study. Section 3 presents the experimental setup and model configuration. The experimental results and discussions are given in section 4. Section 5 summarizes the main findings and outlines directions for future research.

2 Data, Methodology and Assimilation System

2.1 AHI Observation Preprocessing

Himawari-9, a new-generation geostationary satellite operated by the Japan Meteorological Agency (JMA), was launched on 2 November 2016 and is positioned at approximately 140.7 °E. The satellite is equipped with the AHI sensor, which provides full-disk observations every 10 min and can scan target areas at much higher temporal frequencies, ranging from 2.5 min to 30 s. The spatial resolution of AHI varies from 0.5 to 2 km, depending on the spectral band. Such high spatiotemporal-resolution observations are of particular value to monitoring rapidly evolving hazardous weather systems. Besides, AHI consists of 16 spectral bands spanning wavelengths from 0.47 to 13.3 µm, including visible, near-IR, and IR bands. The main characteristics and atmospheric sensitivities of these channels are summarized in Table 1 (Bessho et al., 2016).

In this study, AHI water vapor channels 8-10 and IR window channel 13 were selected for assimilation because of their primary sensitivities to atmospheric moisture and cloud-top properties, respectively. In both the clear-sky and all-sky AHI radiance assimilation experiments, a common set of quality-control (QC) procedures was first applied, including the rejection of observations with satellite zenith angles exceeding 60° and observations whose bias-corrected innovations exceeded three times the prescribed observation error. In the clear-sky assimilation experiment, an additional cloud-detection procedure based on the Himawari-9 AHI Level-2 Cloud Mask product was employed to exclude pixels flagged as cloudy. Furthermore, two additional QC procedures were applied specifically to AHI channel 13, which is primarily sensitive to near-surface thermal emission under clear-sky conditions and to cloud-top information in cloudy scenes. First, to better constrain cloud analyses, only cloud-affected observations with a cloud-effect (CA) index larger than a certain threshold were assimilated in the all-sky channel 13 experiment, as described in Section 2.2. Here, a threshold of 2.0 K was adopted on the basis of preliminary assimilation experiments, while also aiming to retain as much data as possible. Second, channel 13 observations were restricted to oceanic regions to reduce the influence of uncertainties in CRTM land-surface emissivity on window channel radiance simulations. For all experiments, a Gaussian thinning procedure with a 30 km thinning mesh was further applied to reduce potential spatial error correlations among nearby observations (Barker et al., 2012), while also lowering computational cost.

To account for systematic biases in satellite radiance assimilation, a constant bias-correction (BC) scheme was employed. For each channel, the bias was estimated from one month of clear-sky OMB statistics in September 2024 and then applied to both the clear-sky and all-sky assimilation experiments. The resulting values were −0.388, 0.284, −0.630, and −0.660 K for AHI channels 8, 9, 10, and 13, respectively. This BC approach provides an efficient means for initializing bias parameters outside the data assimilation cycle.

Table 1. Characteristics of Himawari-9 AHI infrared channels

Channel	Central wavelength (µm)	Spatial resolution (km)	Physical Properties
7	3.9	2	Low Cloud, Fog, Forest Fire
8	6.2	2	Mid- and Upper- Level Moisture
9	6.9	2	Mid-Level Moisture
10	7.3	2	Mid- and Lower- Level Moisture
11	8.6	2	Cloud Phase, Volcanic SO_2
12	9.6	2	Ozone and potential vorticity
13	10.4	2	Clouds, Cloud Top Information
14	11.2	2	Clouds, Sea Surface Temperature
15	12.4	2	Clouds, Sea Surface Temperature
16	13.3	2	Cloud top height, CO2

2.2 Observation Error Modelling

When assimilating cloud-affected IR radiances, it is essential to calculate observation errors appropriately by considering cloud effects on both the observations C_y and the background C_{xb}. Unlike clear-sky IR radiances, all-sky IR radiances are strongly affected by cloud processes, leading to state-dependent observation error characteristics. To account for these characteristics, the symmetric observation error model proposed by Harnisch et al. (2016) was adopted to modelling AHI observation errors as a function of cloud impact C_{a}, expressed as:

$$C_{\mathrm{a}}=\frac{C_{\mathrm{xb}}+C_{\mathrm{y}}}{2}=\frac{\max\left(0,\mathrm{BT}_{\mathrm{lim}}-\mathrm{Bak}\right)+\max\left(0,\mathrm{BT}_{\mathrm{lim}}-\mathrm{Obs}\right)}{2}. \tag{1}$$

Here Obs is the AHI IR radiance observation and Bak is the simulated all-sky AHI IR radiance from the background. The BT threshold of $\mathrm{BT}_{\mathrm{lim}}$ is determined as the BT differences between the first-guess model equivalent computed without and with clouds. The observation error is then modelled with a piecewise linear function of C_{a} as follows,

$$\left.\begin{array}{ll}\mathrm{SD}=\mathrm{SD}_{\min} & \text{when}\quad C_{\mathrm{a}}\le C_{\mathrm{a}1}\\ \mathrm{SD}=\mathrm{SD}_{\min}+\dfrac{\mathrm{SD}_{\max}-\mathrm{SD}_{\min}}{C_{\mathrm{a}2}-C_{\mathrm{a}1}}(C_{\mathrm{a}}-C_{\mathrm{a}1}) & \text{when}\quad C_{\mathrm{a}1}<C_{\mathrm{a}}<C_{\mathrm{a}2}\\ \mathrm{SD}=\mathrm{SD}_{\max} & \text{when}\quad C_{\mathrm{a}}\ge C_{\mathrm{a}2}\end{array}\right\}. \tag{2}$$

The relationship between observation error and cloud amount are represented with a series of parameters, including the minimum observation errors $\mathrm{SD}_{\min}$, the maximum observation errors $\mathrm{SD}_{\max}$, the minimum cloud amount $C_{\mathrm{a}1}$, and the maximum cloud amount $C_{\mathrm{a}2}$. These parameters were estimated from a one-month of OMB samples, where OMB denotes the difference between the observations and the background-simulated all-sky AHI IR radiances. The resulting parameter values are summarized in Table 2. It is noted that the observation errors for the cloud-sensitive channel 13 are substantially larger than those for the three water vapor channels 8-10. In addition, the upper-level water vapor channel 8, whose weighting function peaks at higher tropospheric altitudes, is less affected by cloud contamination and therefore exhibits smaller observation errors compared to the lower-peaking water vapor channels 9-10. In clear-sky assimilation experiments, constant observation errors of 1.110, 1.058, and 0.915 K were assigned to AHI channels 8-10, respectively.

Table 2. The observation error parameters of Himawari-9 AHI Channels 8-10 and 13

	Minimum cloud amount (K)	**Maximum cloud amount (K)**	**Minimum observation error (K)**	**Maximum observation error (K)**	**Brightness temperature threshold (K)**
Ch 8	0.50	9.50	4.00	15.30	230.5
Ch 9	0.50	13.50	4.60	20.20	240.0
Ch 10	0.50	17.50	3.60	24.00	251.5

Ch 13	0.50	36.00	2.56	40.50	292.0

Figure 1 presents the probability density functions（PDF） of dynamically normalized OMB departures to assess whether the symmetric observation error model yields OMB distributions that are closer to Gaussian curves and thus more consistent with the assumptions of variational data assimilation. Specifically, the OMB samples are first grouped into CA bins with an interval of 1 K, and the OMB departures within each CA bin are normalized by the corresponding bin-wise standard deviation, as follows,

$$\mathrm{OMB}_{\mathrm{norm}}(CA_i) = \frac{\mathrm{OMB}(CA_i)}{\sigma(CA_i)}. \tag{3}$$

Where $\mathrm{OMB}(CA_i)$ represents the OMB departures within the i^{th} CA bin, and $\sigma(CA_i)$ is the corresponding standard deviation estimated for that CA bin. Following Harnisch et al. (2016), this approach accounts for the cloud-dependent heteroscedasticity of observation errors, thereby providing a more appropriate description of OMB PDFs under varying cloud conditions.

As shown in Figure 1, the normalized OMB distributions for all channels are broadly consistent with the Gaussian reference, with the closer agreement found for channels 8-10 within the range of −4 to 4 K. In comparison with the water vapor channels, window channel 13 exhibits a more pronounced deviation from Gaussianity when the absolute normalized OMB value exceeds about 3 K (Figure 1d). This deviation is likely related to larger uncertainties in the simulation of ice-cloud properties and deep convective scenes in all-sky radiative transfer, as well as in the modeling of cloud microphysical processes (Geer et al., 2019; Rendon et al., 2025). Representativeness errors arising from scale mismatches between the observations and the model may further amplify large departures and thus result in the broadened tails (Harnisch et al., 2016). These results suggest that the current linear observation error model may not fully capture the error characteristics of channel 13, for which refined formulations may be required in future studies.

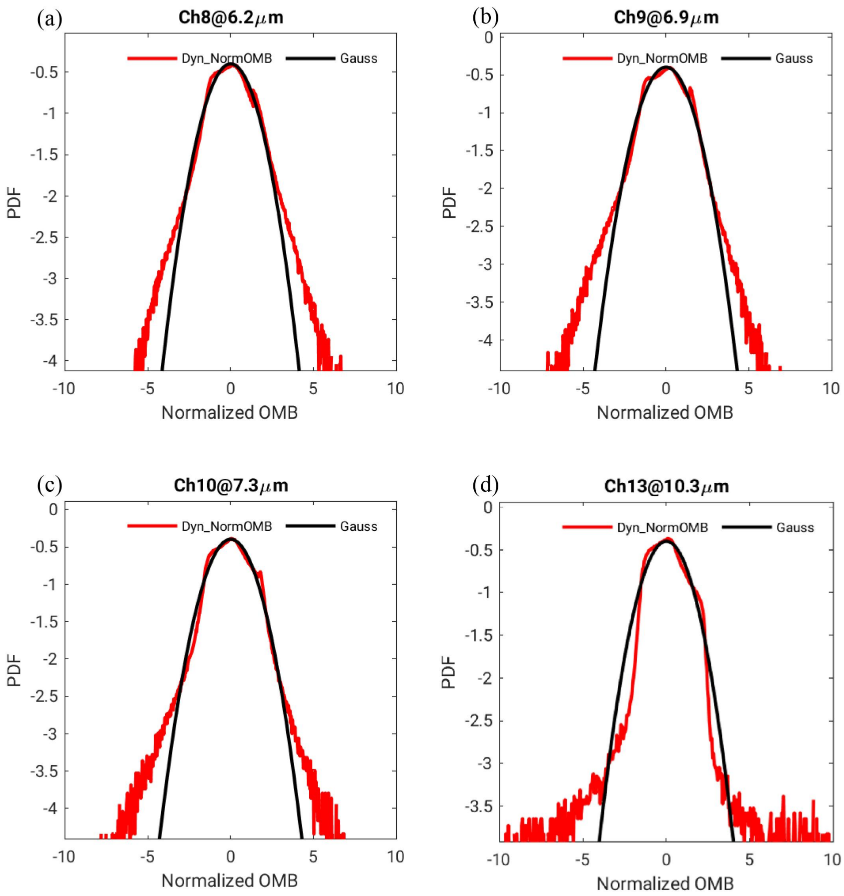

Figure 1. Probability density functions (PDFs) of normalized observation-minus-background brightness temperature (OMB; units: K) for all-sky Himawari-9 AHI (a) Channel 8 (6.2 µm), (b) Channel 9 (6.9 µm), (c) Channel 10 (7.3 µm), and (d) Channel 13 (10.3 µm) brightness temperature (units: K). The black curve denotes the standard Gaussian distribution with *N* (0,1). The statistics were accumulated at 6 hour intervals from 0000 UTC 13 September 2024 to 1800 UTC 12 October 2024.

Figure 2 shows the spatial distributions of observed BT, OMB, and observation error to illustrate how the symmetric observation error model and the quality-control strategies affect the spatial coverage and utilization of assimilated observations. The channel 13 observed BTs lower than ~250 K generally indicate the presence of high cloud tops or vertically deep cloud systems (Figure 2a). In contrast, regions with BTs exceeding 280 K are mostly associated with clear-sky conditions. Figures 2b and 2c show the observation error distributions for channels 13 and 10, respectively, after QC in the all-sky assimilation experiment. For both channels, large observation errors occur predominantly in regions where channel 13 exhibits low BTs (< 250 K), with the error magnitude increasing markedly as BT decreases. These areas also largely coincide with the cloudy scenes identified by the AHI Level-2 cloud mask. Over clear-sky regions where channel 13 BT exceeds about 270 K, the observation errors for both channels are much smaller. This contrast suggests that deep-cloud scenes are more difficult to simulate accurately in the observation operator or the model, whereas uncertainties associated with cloud effects are substantially reduced under less cloudy or cloud-free conditions. It is also noteworthy that the observation errors for channel

https://doi.org/10.5194/egusphere-2026-2982
Preprint. Discussion started: 19 June 2026

13 are generally larger than those for the other water-vapor channels, likely owing to its stronger sensitivity to clouds. For water-vapor channels 8 and 9, the spatial distributions of observation error are broadly similar to that of channel 10 (not shown).

The scatter distributions in Figures 2b and 2c further indicate that channel 13 was subjected to more stringent QC procedures than the water vapor channels, as evidenced by the larger number of rejected observations. For example, samples with normalized OMB below 2 K were excluded. This additional QC step may enhance the effective contribution of cloudy observations during the iterative minimization, while also mitigating potential simulation errors in clear-sky channel 13 associated with uncertainties in surface emissivity. It should also be noted that a portion of the relatively clear-sky samples from channel 13 was currently filtered out using an observation-error-threshold criterion rather than the AHI cloud mask product, which helps retain more observations under less cloudy conditions (Figures 2b and 2f).

Moreover, the all-sky OMB distributions for channels 10 and 13 exhibit pronounced negative departures mainly over oceanic regions where the observations indicate deep cloud systems (Figures 2d and 2e). This negative OMB bias suggests underpredicted cloudiness in the background. The departures are particularly evident for the window channel 13, whose OMB magnitude is larger than that of the water vapor channels. In contrast, large positive departures mostly occur over land under both clear-sky and cloudy conditions, implying that the background predicts excessive moisture and/or clouds. Figure 2f shows the OMB distribution of clear-sky AHI channel 10 observations. The cloudy pixels excluded by the AHI Level-2 cloud mask largely coincide with regions where channel 13 BT is lower than ~260 K, as shown in Figure 2a. In the clear-sky assimilation experiments, a fixed observation error of 0.915 K is assigned and the corresponding OMB departures are comparatively small, within about −3 to 3 K (Figure 2f).

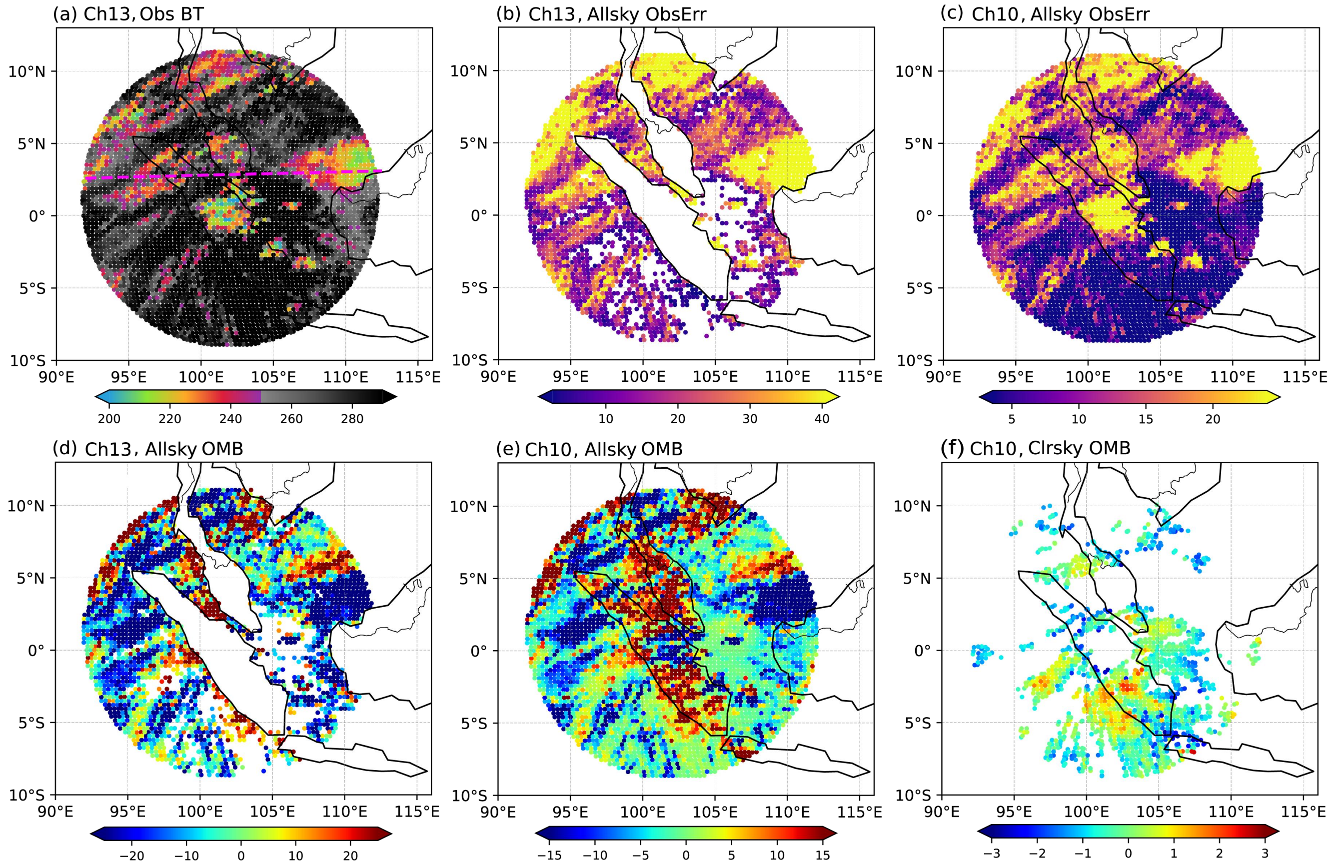

Figure 2. Horizontal distributions of (a) observed brightness temperature (BT; units: K) for AHI channel 13, all-sky observation error (units: K) for (b) channel 13 and (c) channel 10, all-sky observation-minus-background brightness temperature (OMB; units: K) for (d) channel 13 and (e) channel 10, and (f) clear-sky OMB (units: K) for channel 10. All panels are shown for the first assimilation cycle valid at 0600 UTC 23 September 2024.

2.3 MPAS-JEDI Assimilation System

The hybrid ensemble-variational data assimilation experiments in this study were conducted with MPAS-JEDI, which is a new-generation data assimilation system for the MPAS-Atmospheric model (Skamarock et al., 2012, 2018) based on the Joint Effort for Data assimilation Integration (JEDI) framwork (Trémolet and Auligné, 2020; Liu et al.,2022; Guerrette et al.,2023; Jung et al.,2024). In MPAS-JEDI, observations are ingested through the Interface for Observation Data Access (IODA), which provides a unified framework for observation input and storage. The observation operators and QC filters are implemented in the Unified Forward Operator (UFO) of JEDI. For Himawari-9 AHI data, the obs2mpas converter tool was employed to remap Level-1 radiance data and Level-2 cloud products onto the MPAS unstructured mesh. Background-error covariances were represented using the Background Error on Unstructured Mesh Package (BUMP) for ensemble-based background covariances with localization and univariate static background covariances.

For clear-sky and all-sky AHI radiance data assimilation, version 2.4.1 of the Community Radiative Transfer Model (CRTM, Johnson et al., 2023) was used as radiance observation operator. CRTM was further used to compute model-equivalent clear-sky radiances of MHS and all-sky radiances of AHI channels 15-16 for independent verification. The inputs required by CRTM include vertical atmospheric profiles, surface properties, and satellite viewing geometry, with hydrometeor profiles additionally required for all-sky radiance simulations, including cloud liquid water, cloud ice, rain, snow, and graupel. Radar reflectivity observations from a Singapore S-band radar are also used for independent verification of model-simulated reflectivity. After the simulations, two gross QC checks were further applied to exclude observations flagged as poor-quality and to remove outliers.

3 Experimental Configuration

To assess the impact of AHI radiance assimilation over tropical cloudy regions, a set of one-week cycling data assimilation experiments was conducted with MPAS-JEDI. The control experiment (CTL) assimilated only conventional observations with hybrid-3DEnVar, including radiosondes for temperature, zonal and meridional wind components, and specific humidity; aircraft observations for temperature and horizontal wind components; surface observations of surface pressure, 2-m temperature, 2-m specific humidity, and 10-m wind components; atmospheric motion vectors (AMVs) for zonal and meridional wind components; and Global Navigation Satellite System Radio Occultation (GNSS RO) refractivity. Based on the CTL configuration, three additional hybrid-3DEnVar experiments were designed to investigate the effects of assimilating AHI radiances of three water vapor channels under different cloud conditions, as well as the added value of the cloud-sensitive window channel 13. In particular, conventional observations were assimilated together with clear-sky water vapor channels 8-10 radiances in CSR3D, whereas ASR3D assimilated the same observations under all-sky conditions. ASR3D-Ch13 extended ASR3D by additionally assimilating all-sky window channel 13 radiances. Moreover, an ASR4D experiment was conducted to assess the benefit of hybrid-4DEnVar, in which conventional observations and all-sky AHI water vapour channels 8-10 radiances were assimilated, thereby allowing the flow-dependent background error covariance to evolve temporally within the assimilation time window. All experiments were implemented with 6-hourly cycling from 0600 UTC 23 September to 0000 UTC 29 September 2024. For the initial cycle, the background field was provided by a 6 hour spin-up forecast initialized from the ECMWF analyses.

A hybrid background error covariance (BEC) was utilized for all the experiments, comprising 40 % static BEC and 60 % ensemble-based BEC. The ensemble covariance component was estimated from 32-member ensemble forecasts initialized from ECMWF HRES analyses, with the lateral boundary conditions provided by the ECMWF analyses and subsequent forecasts at 3 hour intervals. From 23 to 29 September 2024, the ensemble forecasts were initialized four times per day at 0000, 0600, 1200, and 1800 UTC, and the resulting 6-hour ensemble forecasts were used to construct the ensemble-derived flow-dependent BEC. To reduce sampling errors associated with the limited ensemble size, covariance localization was applied with horizontal and vertical localization scales of 300 km and 4 km, respectively. The static BEC was constructed within the

SABER/BUMP framework, with BUMP_NICAS used to model the spatial correlation structure and variances of each analysis variable, including horizontal wind, temperature, specific humidity, surface pressure, and hydrometeors (cloud liquid water, cloud ice, rainwater, snow, and graupel). In the hybrid-3DEnVar experiment, only ensemble perturbations valid at the analysis time were used, whereas in the hybrid-4DEnVar experiment ensemble perturbations were sampled at 3 hour intervals within the ±3 hour assimilation window.

A 6 hour forecast was launched after each cycling analysis to provide the background for the next assimilation cycle. In addition, 36 hour extended forecasts were initialized every 6 hour from 00:00 UTC 25 September to 00:00 UTC 29 September 2024 to evaluate the short-range forecast performance during a convective precipitation period (Chen et al., 2026). These forecasts were produced using version 8.2.2 of MPAS-Atmospheric model, which employs an unstructured centroidal Voronoi mesh. For each forecast, ECMWF forecast fields were interpolated onto the MPAS mesh to provide the lateral boundary conditions. The model domain was centered over Singapore (1.21175°N, 102.00425°E) and spanned a radius of approximately 1120 km (Figure 2), covering the Malay Peninsula and Indonesia, with a quasi-uniform horizontal grid spacing of about 2.6 km and 522172 grid cells. Vertically, the model comprises 65 levels extending from the surface to 40 km. The MPAS physical parameterizations used in this study include the MYNN schemes for the boundary layer and surface layer (Nakanishi and Niino, 2004, 2009), the WSM6 microphysics scheme (Hong and Lim, 2006), the Grell–Freitas convection parameterization (Grell and Freitas, 2014), the Noah land surface model (Ek et al., 2003), the RRTMG radiation scheme for both shortwave and longwave radiation (Iacono et al., 2008), and the Yonsei University (YSU) boundary layer scheme (Hu et al., 2013). The Xu–Randall scheme was adopted to diagnose cloud fraction for radiation (Xu and Randall, 1996).

4 Results and Discussion

4.1 Impacts on Analysis and Background Fields

Figures 3 and 4 present the vertical cross sections of humidity and hydrometeor analysis increments from the first assimilation cycle, for which all experiments were initialized with the same background state. Over the land region near 99–104°E, more negative humidity increments are produced by three all-sky/ASR experiments (Figures 3b-d) in response to the positive OMB departures shown in Figure 2c. By contrast, CSR3D exhibits a clear-sky OMB pattern dominated by negative departures (Figure 2e), and its analysis increments tend to increase the model humidity (Figure 3a). Besides, over the cloudy regions near about 95 °E and 109 °E, the humidity increments in CSR3D are much weaker than those in the other ASR experiments (Figures 3b-d), since no AHI observations were assimilated there. The observed cloud-top pressure, denoted by the black dashed line, is generally distributed between 100 and 250 hPa, suggesting the presence of upper-level and/or vertically deep cloud systems. In these cloudy regions, CSR3D, which assimilates only clear-sky observations, exhibits no hydrometeor increments and thus fails to reproduce the observed cloudy structures within the red-boxed region in Figure 3a. In the other all-sky experiments, more positive hydrometeor increments are generated between 300 and 700 hPa in these regions, leading to simulated cloud-top heights that are in better agreement with the observations (Figure 4).

https://doi.org/10.5194/egusphere-2026-2982
Preprint. Discussion started: 19 June 2026

The primary differences among the three ASR experiments are concentrated within the semi-transparent or less cloudy region near 104–108.4°E, where positive and negative OMB departures occur simultaneously (Figures 2a and 2e). Over this area, ASR3D yields more pronounced negative humidity increments (Figure 3b), while generating limited positive hydrometeor increments (Figures 4a and 4d). By comparison, both ASR3D-Ch13 and ASR4D are characterized primarily by weaker positive humidity increments accompanied by stronger positive hydrometeor increments (Figures 4b-c and 4e-f). Similar differences are also evident in other regions of vigorous cloud development, where ASR3D generally exhibits smaller hydrometeor increments than ASR3D-Ch13 and ASR4D (Figure 4). This may reflect the fact that the additional cloud-sensitive observations assimilated in ASR3D-Ch13 enables the observed information to be projected more efficiently onto the hydrometeor variables during the iterative minimization. For ASR4D, the more complete adjustment of hydrometeor control variables is likely attributable to the combined effects of flow-dependent background-error covariances and the explicit use of temporal evolution information within the assimilation window. Another notable difference among the all-sky experiments lies in the analyzed cloud-top height. As highlighted by the orange box in Figure 4b, ASR3D-Ch13 produces a lower cloud-top height that is more consistent with the observed vertical cloud structure than those in the other experiments. Meanwhile, the larger positive hydrometeor increments generated by ASR3D-Ch13 around 400 – 600 hPa likely increase the optical thickness and effective emissivity of the mid-tropospheric cloud layer (Figures 4b and 4e).

To further assess the consistency between the analysis fields and observations, the corresponding distributions of all-sky observation-minus-each experiment analysis (OMA) BT departures are presented in Figures 3e and 3f for AHI channels 10 and 13, respectively. The results for channels 8-9 exhibit similar behaviors and are therefore not shown. The consistently larger OMA departures in channel 13 relative to channel 10 indicate the greater difficulty of fitting cloud-sensitive window channel observations. Since only clear-sky observations are assimilated in CSR3D, it exhibits the largest difference between the observed and analyzed all-sky BTs, particularly for channel 13 over the cloudy regions near 95°E and 109°E. This result is consistent with the distribution of analysis increments discussed above. In contrast, three ASR experiments generally yield smaller OMA departures, suggesting an improved fit to the observations. Among them, ASR3D-Ch13 shows the best overall performance, implying that the associated humidity and hydrometeor increments more effectively adjust the analysis state toward the all-sky observations. Notably, ASR4D exhibits slightly larger OMA departures than ASR3D in some regions. This behavior may be attributed to the temporal constraints introduced by the 4DEnVar framework, which distribute observational information more smoothly across the assimilation window rather than maximizing the fit to observations at a single analysis time.

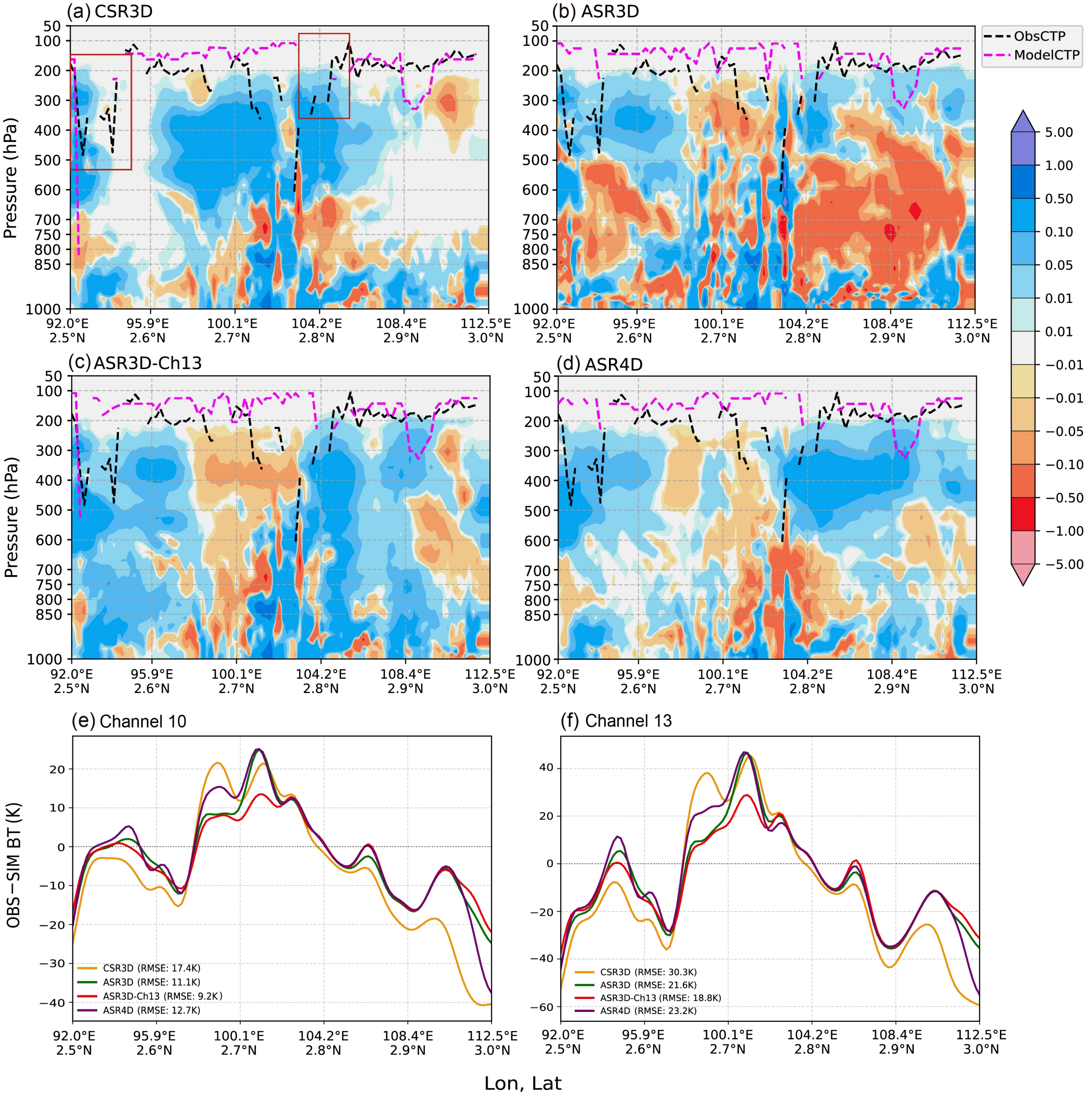

Figure 3. Vertical cross sections of water vapor mixing ratio (shading; units: g·kg⁻¹) analysis increment from the (a) CSR3D, (b) ASR3D, (c) ASR3D-Ch13 and (d) ASR4D experiments along the transect shown in Figure 2a. The black and magenta dashed lines denote the observed and model-simulated cloud-top pressure (units: hPa), respectively. The corresponding distributions of all-sky observation-minus-each experiment analysis (OMA, units: K) brightness temperature departures for AHI (e) channel 10 and (f) channel 13, respectively, with root-mean-square errors denoted in the legend. All panels are shown for the first assimilation cycle valid at 0600 UTC 23 September 2024.

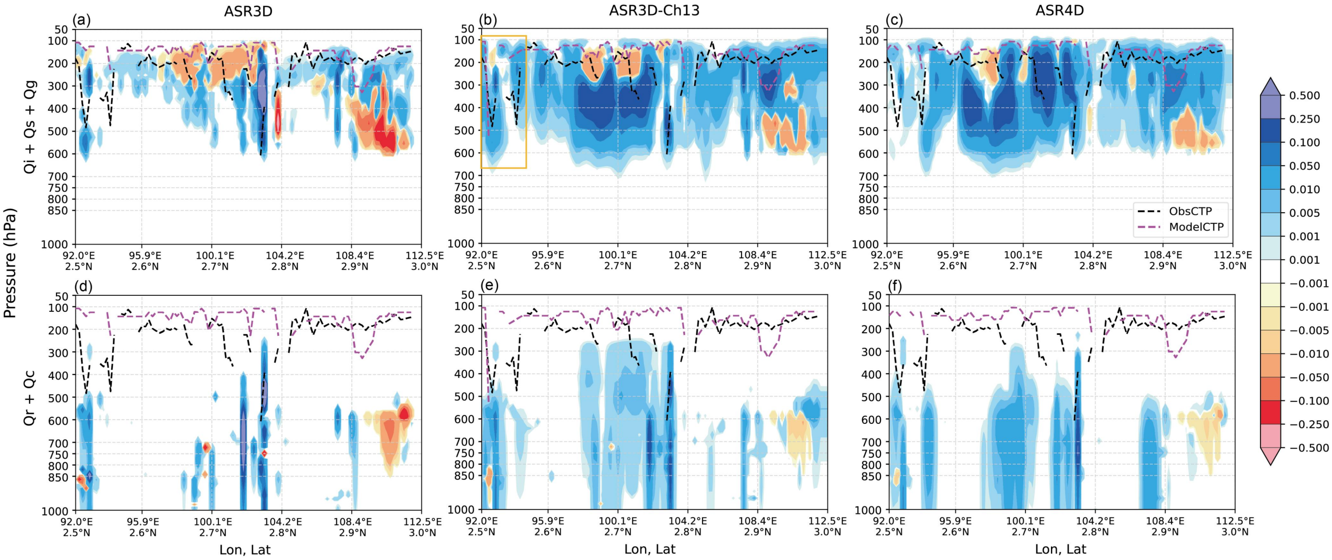

Figure 4. Vertical cross sections of hydrometeor mixing ratio (shading; units: g·kg^{-1}) analysis increment along the transect shown in Figure 2a for the (a, d) ASR3D, (b, e) ASR3D-Ch13, and (c, f) ASR4D experiments, including the total condensate of cloud ice, snow, and graupel in the first row and that of cloud water and rain in the second row. The black and magenta dashed lines denote the observed and model-simulated cloud-top pressure (units: hPa), respectively. All panels are valid for the first assimilation cycle at 0600 UTC 23 September 2024.

OMB statistics derived from two non-radiance observing systems, GNSS-RO refractivity and satellite-derived Atmospheric Motion Vectors (AMVs), are further examined to assess background-field quality during the cycling assimilation period. Compared with soundings, these data provide a larger number of effectively assimilated samples (not shown). Figure 5 shows the percentage differences in the root-mean-square error (RMSE) of GNSS-RO refractivity OMBs for each experiment relative to CTL. The negative value indicates reductions in RMSE relative to CTL and hence improved performance, whereas the positive value indicates degradation. Because GNSS-RO refractivity is highly sensitive to lower-tropospheric moisture and to temperature in the middle and upper troposphere, these statistics provide a useful indicator of the thermodynamic quality of backgrounds.

As shown in Figure 5a, the RMSE differences in the AHI assimilation experiments are largely within −8 % to 3 % throughout the cycling period, with the largest reduction exceeding −10 %. This suggests that all-sky AHI assimilation exerts a generally neutral-to-positive influence on the thermodynamic structure of the background field over time. Consistent with this result, Figure 5b shows that the AHI assimilation experiments generally produce negative RMSE differences across the 4–15 km layer, with reductions reaching approximately 5–15 % at several lower-tropospheric levels, indicating an overall beneficial effect relative to CTL. Among the AHI radiance assimilation experiments, the ASR3D-Ch13 and ASR4D experiments generally outperform the other experiments during most assimilation cycles, especially below 15 km. The improvements in ASR3D-Ch13 are predominantly found below 7 km and remain comparatively stable throughout the cycling period, which suggests a persistent benefit to the lower-tropospheric thermodynamic structure. After 0000 UTC 27 September

2024, ASR4D gradually exhibits the greatest improvement, with its largest reductions occurring between 7 and 15 km in the middle-to-upper troposphere.

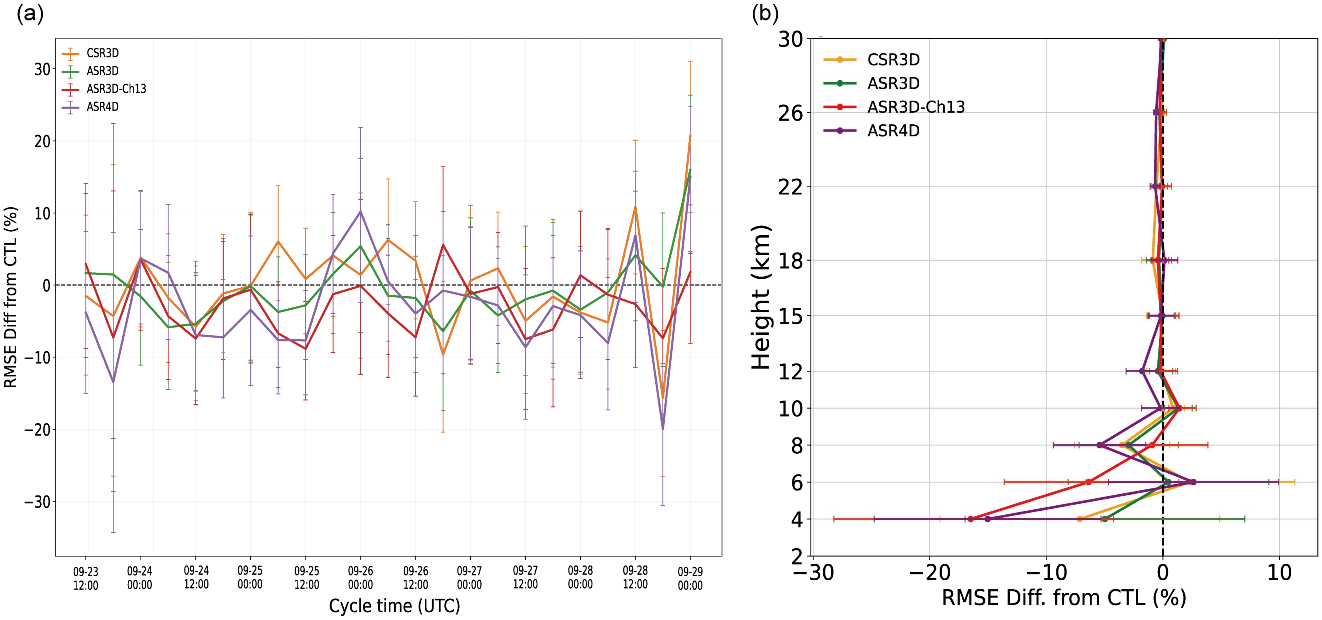

Figure 5. (a) Time series of percentage differences in the root-mean-square error (RMSE; units: %) of GNSS-RO refractivity observation-minus-background (OMB; units: N) relative to CTL for the CSR3D, ASR3D, ASR3D-Ch13, and ASR4D experiments during the cycling assimilation period. (b) Corresponding vertical profiles of the time-averaged RMSE percentage differences relative to CTL. Error bars denote the 90% confidence intervals. Statistics are calculated from 1200 UTC 23 September to 0000 UTC 29 September 2024 at 6 hour intervals.

Figure 6 shows the OMB statistics of AMVs, which are used to evaluate the impact of different AHI assimilation strategies on the background wind field. Relative to CTL, all AHI assimilation experiments exhibit more evident improvements in the meridional wind (V-wind) component across most levels between 250 and 1000 hPa, with averaged RMSE reductions of approximately 5% (Figure 6a). Among these experiments, the largest positive effects are observed in ASR4D and ASR3D-Ch13, primarily in the upper and lower troposphere, respectively. The results suggest that the cycling assimilation of all-sky AHI radiances tends to progressively enhance the background V-wind field, which is likely associated with the propagation of improved thermodynamic and cloud-related analyses into the V-winds via model dynamical adjustment within the Hybrid-EnVar framework. By contrast, the AHI assimilation experiments show an overall neutral impact on the background zonal wind (U-wind) field, with most RMSE differences confined within ±10% across the troposphere (Figure 6b). More specifically, relative to CTL, CSR3D and ASR3D exhibit comparatively larger RMSE reductions at most levels, whereas ASR3D-Ch13 and ASR4D show larger RMSEs than CTL below 600 hPa.

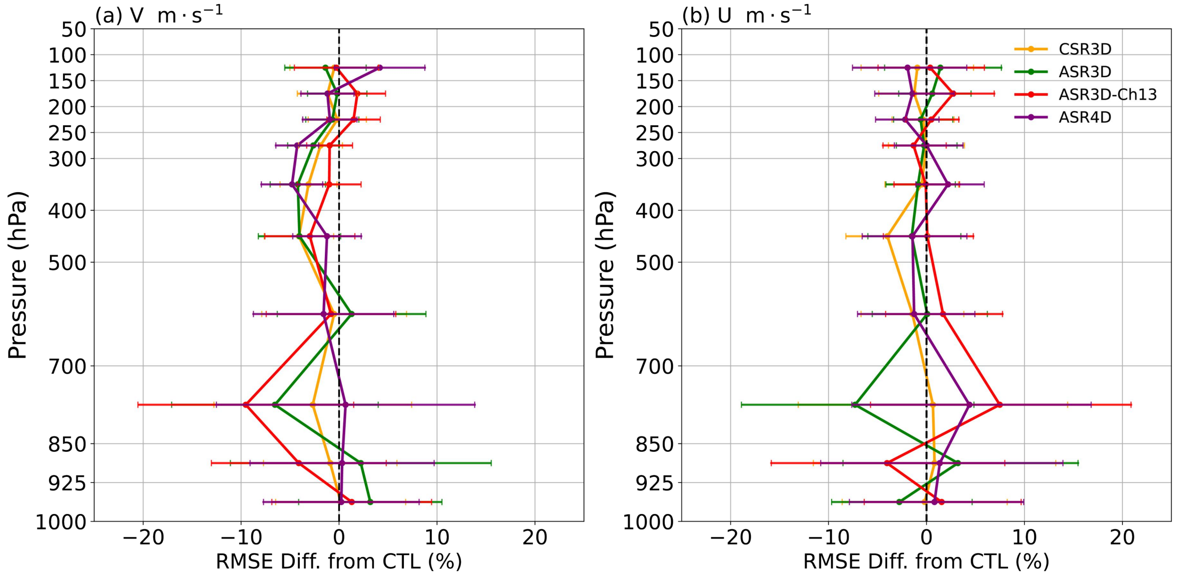

Figure 6. Vertical profiles of percentage differences in observation-minus-background (OMB) root-mean-square error (RMSE; units: %) for Atmospheric Motion Vector (AMV) (a) meridional and (b) zonal wind components (units: m·s⁻¹) in the CSR3D, ASR3D, ASR3D-Ch13, and ASR4D experiments, relative to CTL. Vertical statistics are shown as layer-mean values by averaging all samples located between two adjacent pressure levels. Error bars represent the 90 % confidence intervals. Statistics are computed from 1200 UTC 23 September to 0000 UTC 29 September 2024 at 6 hour intervals.

To further assess the accuracy of the background humidity field, independent verification was performed using the clear-sky radiances from Metop-B MHS channel 4 (183.31 ± 3 GHz), which were not assimilated and are primarily sensitive to the middle- and upper-tropospheric humidity. Figures 7a-e present the horizontal distributions of MHS observation-minus-simulated BTs based on the 6 hour background forecast (OMF) for a representative case with relatively dense MHS coverage. Figure 7f further shows the probability density functions of observed and model-simulated BTs from the five experiments, aggregated over multiple times. These diagnostics provide a comprehensive characterization of humidity forecast errors in terms of their spatial pattern and systematic statistical behavior.

As shown by the OMF spatial distributions in Figures 7a-e, CTL exhibits the largest OMF, with a mean value of −1.65 K. Most negative OMF departures are concentrated in cloudy regions, consistent with a dry bias in the background field. Positive departures, by contrast, are located primarily in clear-sky regions, suggesting excessive atmospheric moisture in the background. Relative to CTL, all AHI radiance assimilation experiments reduce both negative and positive biases, with the mean OMF decreasing by about 0.22, 0.18, 0.36, and 0.34 K for CSR3D, ASR3D, ASR3D-Ch13, and ASR4D, respectively. Among these experiments, ASR3D-Ch13 and ASR4D exhibit relatively smaller negative OMFs over cloudy regions (Figures 7d-e), highlighting their enhanced ability to alleviate the dry bias, likely via stronger positive humidity increments (Figure 3c). The horizontal distributions further suggests that ASR3D is more effective in reducing positive OMFs and mitigating the moist forecast bias in clear-sky regions (Figure 7c). This improvement is likely related to the larger negative humidity increments in its analysis field (Figure 3b), which suppress excessive moisture and result in a drier subsequent forecast.

https://doi.org/10.5194/egusphere-2026-2982
Preprint. Discussion started: 19 June 2026

The probability density functions in Figure 7f further corroborate the above results. A clearly right-skewed distribution is evident in CTL relative to the observations, with the largest negative mean bias around −0.58 K, indicating that the largest dry bias occurs in its background field. Relative to CTL, all AHI assimilation experiments shift the simulated BTs closer to the observed distribution, with reduced mean biases. In addition, CSR3D exhibits larger negative BT biases than the other ASR experiments, especially in the left tail for BTs below ~256 K. These results suggest that all-sky assimilation of AHI radiances is more effective than clear-sky assimilation in improving the background humidity. Among the all-sky experiments, ASR3D-Ch13 shows the closest agreement with the observed distribution and the smallest mean bias (−0.58 K), particularly for BTs above ~259 K.

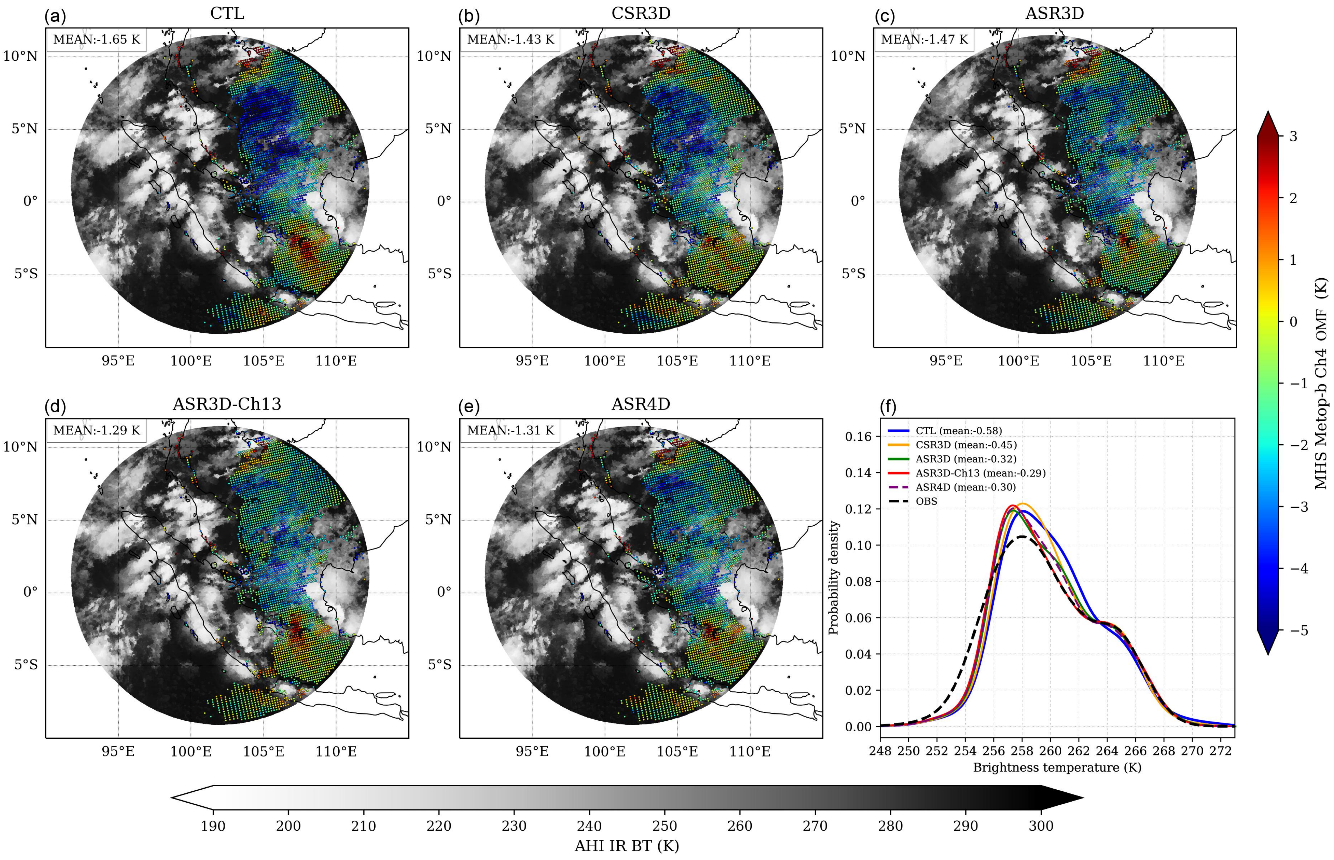

Figure 7. Spatial distributions of AHI channel 13 (10.4 µm) observed brightness temperature (grayscale shading; units: K) and MHS Metop-B channel 4 (183.31 ± 3 GHz) observed-minus-background simulated brightness temperature based on the 6 hour forecast (OMF; scatters; units: K) of (a) CTL, (b) CSR3D, (c) ASR3D, (d) ASR3D-Ch13, and (e) ASR4D experiments, valid at 1200 UTC 27 September 2024. (f) The probability density function of Metop-B MHS channel 4 brightness temperatures from observations and the corresponding model-simulated values for the five experiments, with the mean bias denoted in the legend. The PDF statistics are calculated from 1200 UTC 23 September to 0000 UTC 29 September 2024 with a 6 hour interval.

https://doi.org/10.5194/egusphere-2026-2982
Preprint. Discussion started: 19 June 2026

4.2 Impacts on short-range Forecasts

To further assess the impacts of the different experiments on short-range cloud forecasts, independent BT-space *HofX* verification was performed using all-sky radiances from AHI channels 15 (12.4 µm) and 16 (13.3 µm), which were excluded from the assimilation. Both channels are highly sensitive to upper-level ice clouds, cirrus, and cloud-top height. The evolution of OMF RMSE over the 1–6 hour forecast range is shown in Figure 8, where OMF is defined as the difference between the observed AHI BT and the corresponding simulated BT from each experiment's forecast. In Figures 8c-d, the negative percentage differences indicate improved performance relative to CTL, whereas positive values indicate degradation.

As shown in Figures 8a and 8b, CTL yields RMSE values of ~23.4 K for channel 15 and ~18.2 K for channel 16 at the 1 hour forecast lead time. The larger RMSE in channel 15 likely reflects its less clean window-channel character relative to channel 16, such that its radiances maybe influenced not only by cloud-related signals but also by the atmospheric temperature and humidity information. Compared to CTL, the experiments that assimilate AHI radiances generally have lower RMSE values over the entire 1–6 hour forecast range, with the most pronounced improvement evident at the 1 hour lead time. This early improvement signal, evident even within the spin-up period, suggests that the AHI radiance assimilation promotes a faster adjustment of the cloud forecast through a more accurate initial condition.

Among the AHI assimilation experiments, ASR4D performs best and retains this advantage through most of the 1–6 hour forecast range. For channel 15, the largest RMSE reduction is achieved by ASR4D, reaching about 5.0 % relative to CTL at hour 1, whereas for channel 16 the improvement is even greater, with RMSE reductions of about 5.8 %–6.0 % (Figures 8c-d). Compared with ASR3D, ASR3D-Ch13 performs better during the first 1–3 hour, with improvements generally ranging from 4.5 % to 6.0 %. However, this advantage diminishes after 3 hours, and its performance gradually becomes inferior to that of ASR3D. Although CSR3D also shows positive impacts relative to CTL, its benefit remains clearly smaller than that of the other three all-sky assimilation experiments.

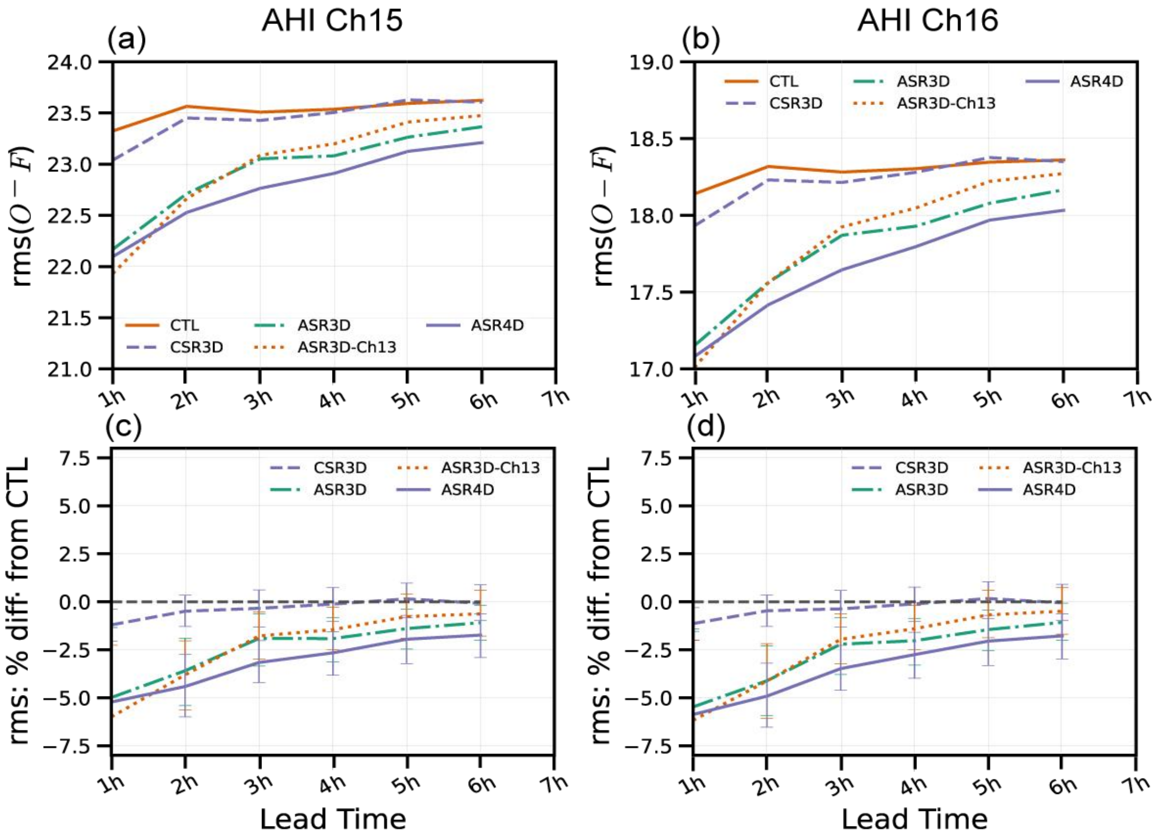

Figure 8. Root-mean-square error (RMSE) of AHI observation-minus-model simulated brightness temperature base on the 1-6 hour forecasts (OMF, units: K) as a function of lead time for (a) channel 15 and (b) channel 16, along with (c, d) the corresponding percentage differences relative to CTL for CSR3D, ASR3D, ASR3D-Ch13, and ASR4D. Statistics are computed from 1200 UTC 23 September to 0000 UTC 29 September 2024 with a 6 hour interval. Error bars denote the 90 % confidence intervals.

Figure 9 shows contoured frequency by altitude diagrams (CFADs) of observed radar reflectivity and the corresponding *MPAS*-simulated reflectivity based on the 12 hour forecasts from each experiment. The independent observations are from a S-band radar over Singapore, with a selected case characterized by a relatively complete distribution of convective echoes. This diagnostic enables a direct assessment of differences among the experiments in predicting the vertical structure of precipitation-related hydrometeors.

According to the observations, the high reflectivity frequencies are mainly concentrated between ~20–37 dBZ at altitudes of ~1–3 km, indicating that precipitating hydrometeors are primarily confined to the lower and middle troposphere (Figure 9a). Above about 3 – 4 km, radar echoes become less frequent, with reflectivity values mostly remaining below 35 dBZ. Compared with the observations, CTL exhibits clear biases in the vertical distribution of reflectivity (Figures 9a-b). Specifically, CTL exhibits a broader high-frequency distribution of 25–30 dBZ reflectivity, and the vertical extent of its simulated 30 dBZ echoes is clearly larger than observed, with echo tops extending above 4 km. This suggests that CTL tends to overpredict the vertical development of convection systems, as well as the associated hydrometeor loading. By contrast, these biases are mostly alleviated in the other AHI assimilation experiments, in which the frequency core at 25–30 dBZ and 1–3 km agrees more closely with the observations (Figures 9c-f).

Among the AHI assimilation experiments, ASR3D-Ch13 and ASR4D tend to better capture the pattern of the high-frequency core (> 0.8%). By contrast, CSR3D and ASR3D show suboptimal performance, characterized by reflectivity values exceeding 25 dBZ that form an unrealistic downward-tilted structure relative to the observations. The limited sensitivity of AHI water-vapor channel assimilation to precipitating hydrometeors likely contributes to this deficiency. Furthermore, a slight shift toward lower reflectivity values is noticed in most of the experiments relative to the observations, which may indicate a tendency to underpredict hydrometeor particle sizes or reflect spatial displacement errors in the simulated convective systems.

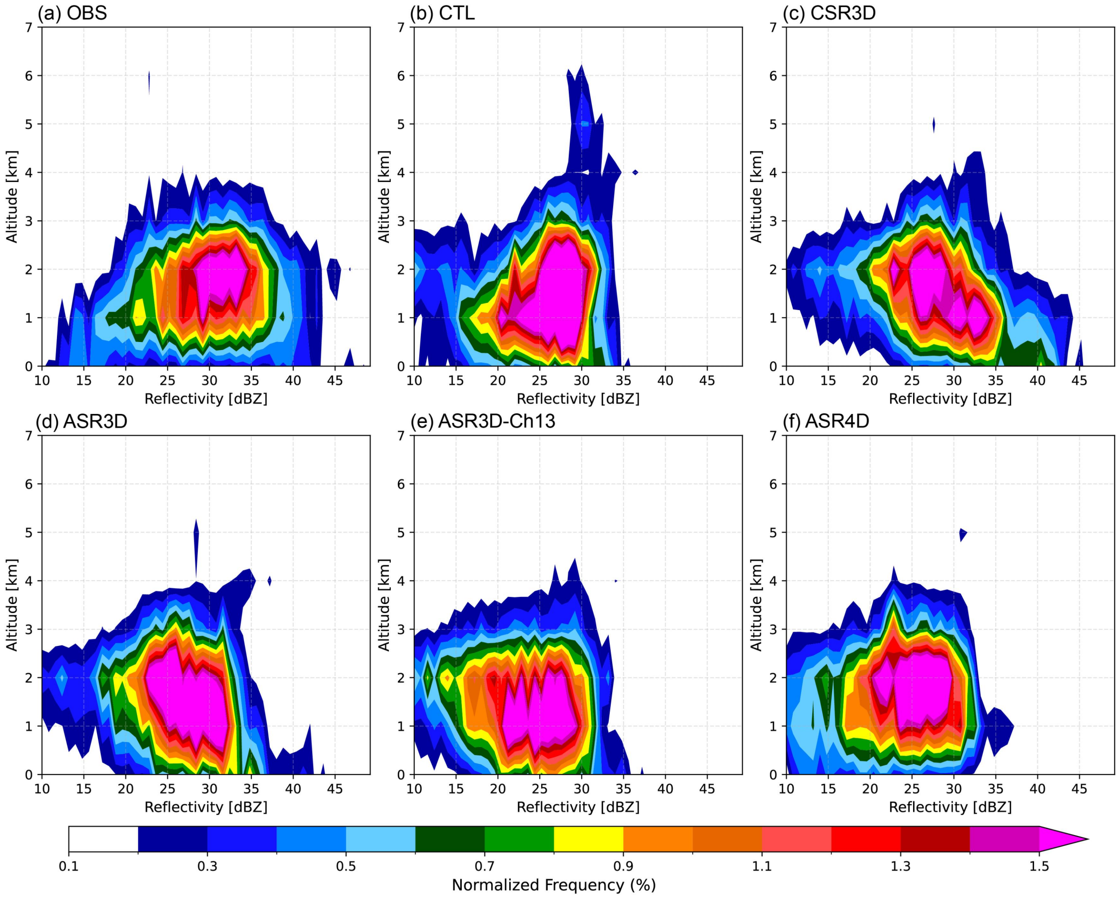

Figure 9. Contoured frequency by altitude diagrams (CFADs) of S-band radar reflectivity (units: dBZ) versus altitude (units: km) for (a) the observations and the corresponding model simulations based on 12 hour forecasts from (b) CTL, (c) CSR3D, (d) ASR3D, (e) ASR3D-Ch13, and (f) ASR4D, valid at 0000 UTC 26 September 2024. Shading denotes normalized frequency (units: %).

Figure 10 presents the Fraction Skill Score (FSS) for 3 hour accumulated precipitation over the 36 hour forecast period for all experiments, together with the relative differences of the AHI assimilation experiments with respect to CTL. In Figure 10b, performance is improved relative to CTL where percentage differences are positive, while degradation is associated with negative values. Forecast skill is evaluated using a percentile-threshold approach that assesses the ability to reproduce the

https://doi.org/10.5194/egusphere-2026-2982
Preprint. Discussion started: 19 June 2026

spatial distribution of the main precipitation regions (Roberts and Lean, 2008; Nystrom et al., 2025). At a given spatial scale, precipitation forecasts are considered skillful when the FSS exceeds a reference value determined from the scenario, in which all grid cells have an equal probability of exceeding the specified 95% threshold. The FSS is calculated using a 5x5-grid-point neighbourhood window, for which a value of 1 indicates a perfect forecast. The observations are obtained from hourly IMERG precipitation on a 0.1° latitude–longitude grid and accumulated into 3 hour totals, while the MPAS 3-hour accumulated precipitation forecasts are interpolated to the same grid prior to verification.

Figure 10a shows that all experiments share a similar temporal evolution in absolute FSS, with values increasing from 3 to 18 hour and then declining as forecast lead time increases further. The increase in FSS during the first 18 hour can be partly attributed to a period of spin-up during which the model adjusts from the initial conditions toward a dynamically balanced state (Done et al., 2004). In addition, the impact of all-sky radiance assimilation is often indirect, acting first on humidity and cloud variables and only later affecting precipitation processes through the dynamical evolution of the model (Bannister, 2017; Geer et al., 2019). The subsequent decrease in FSS is likely associated with the accumulation of forecast errors and the inherently limited predictability of convective-scale precipitation systems. The FSS reaches its maximum at 18 hour, with peak values ranging from approximately 0.42 to 0.52 across the experiments.

Relative to CTL, the AHI assimilation experiments further improve precipitation forecast skill, particularly the three all-sky experiments, whose positive effects persist through most of the first 33 hour, with relative improvements of about 5 %–40 % (Figure 10b). Based on the same all-sky hybrid-3DEnVar framework, ASR3D-Ch13 outperforms ASR3D during the first 12 forecast hours, with improvements of up to approximately 38%. This result suggests that assimilating additional cloud-sensitivity channel 13 primarily improves forecast skill scores at early lead times, possibly because the associated analysis increments more effectively adjust the initial cloud and hydrometeor fields. Although the 3D hybrid experiments generally further improve forecasts at short lead times, the superiority of ASR4D becomes evident after 12 hours and retains the lowest errors thereafter until 27 hours. This likely reflects the greater ability of four-dimensional assimilation to constrain the time-evolving model state, thereby alleviating initial dynamical imbalances and allowing the positive impact to be maintained over a longer forecast period. In contrast, CSR3D, which assimilates only clear-sky observations, shows the smallest improvement among the AHI assimilation experiments. Its error reductions remain modest, generally within 5% at most lead times, while the forecast error even increases by ~9% at the 9 hour lead time.

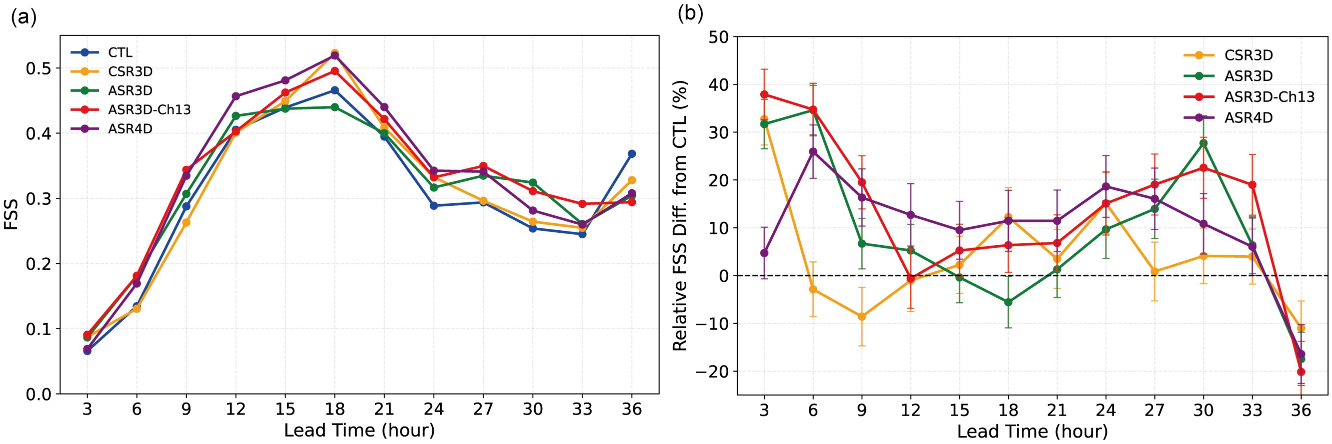

Figure 10. (a) Fraction skill scores (FSS) for 3 hour accumulated precipitation as a function of forecast lead time from 3 to 36 hour, and (b) relative FSS differences (units: %) with respect to CTL for CSR3D, ASR3D, ASR3D-Ch13, and ASR4D. 17 forecast samples are initialized at 6 hour intervals from 0000 UTC 25 September to 0000 UTC 29 September 2024. Error bars denote the 90 % confidence intervals.

Figure 11 shows the spatial distribution of observed and 18–24 hour lead time forecasts of 6 hour accumulated precipitation during a representative heavy-rainfall period, together with the vertically integrated water vapour transport (IVT) from 1000 to 200 hPa represented by black streamlines. The IVT statistic is calculated as follows:

$$IVT = \frac{1}{g}\int_{1000}^{HPL} q\sqrt{u^2 + v^2}\,dp \qquad (4)$$

where g is the gravitational acceleration, set to 9.81 m·s^{-2}; HPL is the upper pressure level, specified as 200 hPa in this study; q is the specific humidity (kg·kg^{-1}); u and v represent the zonal and meridional wind components, respectively; p is the pressure level.

According to the observations, the main precipitation regions can be divided into three areas, as denoted by black boxes 'A-C' in Figure 11a, which correspond to convective cores located over the ocean and along the coastal transition zone. In all experiments, the predicted precipitation distributions are broadly consistent with the observed patterns. However, in areas where the observed precipitation is below 30 mm, the rainfall intensity is substantially overpredicted in all experiments, which may indicate a systematic bias in the model (Chen et al., 2026).

Compared with the other AHI assimilation experiments, CTL exhibits larger forecast errors, which are characterized by an underestimation of the spatial extent of precipitation exceeding 10 mm, particularly in regions 'A' and 'C' (Figure 11b). This spatial deficiency is likely related to inadequate moisture transport, as reflected by the relatively sparse and less coherent IVT streamlines in CTL (red boxes in Figure 11b). After assimilating AHI radiances, all experiments exhibit improved forecasts of precipitation distribution relative to CTL. Although the three all-sky experiments show comparable skill in predicting rainfall intensity, ASR4D yields a more accurate precipitation distribution over region 'C'. This result is consistent with the previous FSS-based assessment and further indicates that four-dimensional variational assimilation is more beneficial for improving the prediction of rainfall distribution at longer forecast lead times. Conversely, the improvement achieved by CSR3D under the clear-sky assimilation framework remains inferior to that of the all-sky AHI assimilation experiments, especially in region 'C' related to the coastal and adjacent land areas between 2.5 °S and 5 °S (Figures 11c-f).

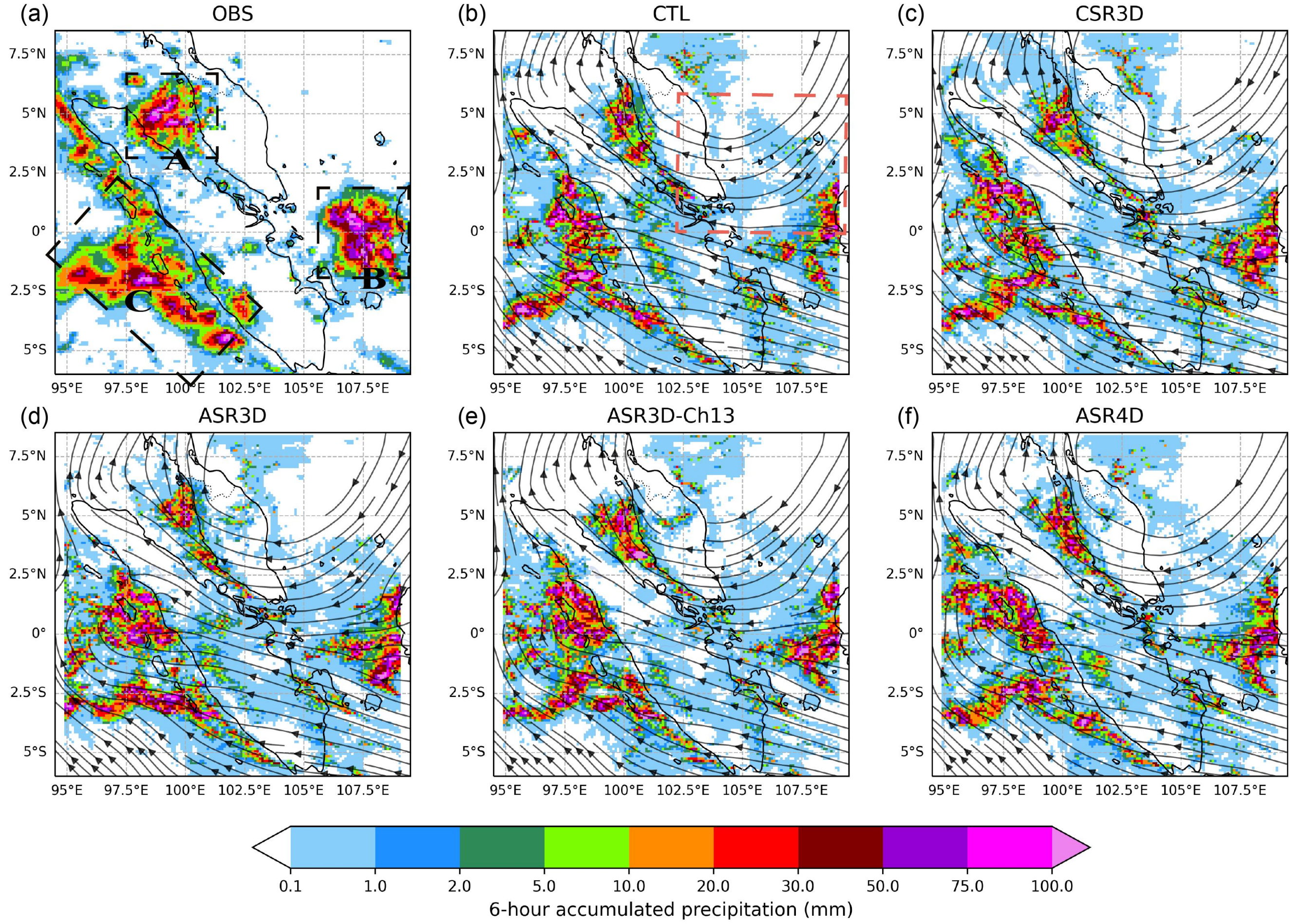

Figure 11. Horizontal distributions of 6 hour accumulated precipitation (shading; units: mm) from (a) the IMERG observations and 18-24 hour lead time forecasts of (b) CTL, (c) CSR3D, (d) ASR3D, (e) ASR3D-Ch13, and (f) ASR4D, together with the vertically integrated water vapour transport from 1000 to 200 hPa (black streamlines, units: kg·m^{-1}·s^{-1}) averaged over 6 hour. The forecasts are valid from 1800 UTC 28 to 0000 UTC 29 September 2024.

5 Summary

This study investigated the impacts of Himawari-9 AHI all-sky infrared radiance assimilation on short-range cloud and precipitation forecasts over the Maritime Continent using a convection-permitting, high-resolution regional MPAS model. Both AHI water vapor and window channels are jointly assimilated within the hybrid-3D/4DEnVar framework. Based on five one-week cycling assimilation sensitivity experiments, the results were systematically evaluated in the analysis, background, and forecast fields, along with verification against multiple types of independent observations. The main findings are summarized as follows.

Analysis diagnostics indicate that, within cloudy regions, CSR3D, which assimilates only clear-sky AHI observations, has no hydrometeor increments and therefore exhibits larger errors in the analyzed cloud-top structure and a degraded fit to the all-sky observed BTs. By comparison, stronger hydrometeor increments are generated in the all-sky AHI assimilation experiments, leading to analyzed BTs and cloud-top heights that are more consistent with the observations, particularly in ASR3D-Ch13.

Background-field evaluation using multiple types of observations indicates that AHI radiance assimilation has an overall neutral-to-positive impact on background quality relative to CTL. Specifically, verification against GNSS-RO refractivity shows reduced thermodynamic errors throughout the 4–15km layer, with the largest benefits in ASR3D-Ch13 over the mid-troposphere and in ASR4D over the upper troposphere. The AMV-wind verification further indicates that improvements are more pronounced for the meridional than for the zonal wind component, with RMSE reductions reaching approximately 5% and ±10%, respectively. Besides, independent MHS channel 4 verification shows that all-sky AHI assimilation provides a more accurate background humidity field than CTL and clear-sky AHI assimilation.

Forecast verification against independent AHI window channels 15-16 observations indicates that, relative to CTL and CSR3D, the all-sky AHI assimilation experiments exhibit greater improvements in short-range forecasts of upper-level ice clouds or cloud-top structures, with ASR4D yielding the best overall performance. Independent radar reflectivity verification further suggests that ASR3D-Ch13 tends to better predicts the observed high-frequency reflectivity core, implying that window channel 13 may provide additional benefit for representing precipitation-related hydrometeors within convective systems. Moreover, the all-sky AHI assimilation experiments generally exhibit higher skill in predicting the spatial distribution of heavy rainfall. In particular, assimilating the additional cloud-sensitive channel 13 radiances enhances forecast skill during the first 12 hour, whereas the four-dimensional assimilation framework provides more sustained benefits at longer lead times.

Although this study demonstrates the feasibility and potential value of all-sky geostationary infrared radiance assimilation in the MPAS-JEDI system for tropical short-range forecasting, several issues still warrant further investigation. First, while the assimilation of cloud-sensitive window channel 13 provides added value for cloud and precipitation analyses, its larger and more non-Gaussian observation errors point to the need for further refinement of observation-error modeling, along with the development of cloud-scene-dependent quality-control strategies. Given the simultaneous assimilation of multiple water-vapor channels, inter-channel error correlations should likewise be more carefully represented and optimized in future work. In addition, future work could further examine the complementary roles of cloud-sensitive window channels and four-dimensional hybrid assimilation. The former may support rapid adjustment of cloud and hydrometeor structures, whereas the latter may help maintain these benefits through improved temporal consistency. To facilitate the practical implementation of such approaches, dual-resolution assimilation strategies could also be explored as a means of improving computational efficiency.

Code and Data Availability

The source code of MPAS-JEDI version 3.0.3 is archived on Zenodo at https://doi.org/10.5281/zenodo.19209009 (last access: 10 May 2026; JCSDA and NCAR, 2025). The MPAS-Atmosphere version 8.2.2 and the CRTM version 2.4.1 are also available via Zenodo at https://doi.org/10.5281/zenodo.13821326 (last access: 10 May 2026; Duda et al. 2024) and https://doi.org/10.5281/zenodo.7823722 (last access: 10 May 2026; Johnson et al., 2023), respectively. The Himawari-9 AHI L1 Full Disk radiances and L2 cloud retrieval products were produced and managed by the Japan Meteorological Agency (JMA) and accessed through the NOAA Himawari Open Data service, available at: https://registry.opendata.aws/noaa-himawari/ (last access: 10 May 2026; JMA and NOAA, 2026). Historical Himawari Standard Data are also available via the JAXA Himawari Monitor/P-Tree system, a JMA-related archive service: https://www.eorc.jaxa.jp/ptree/index.html (last access: 10 May 2026; JAXA, 2026). The ADP Global Upper Air and Surface Weather Observations (PREPBUFR format) and NCEP GDAS Satellite Data are available from the NCAR Research Data Archive (RDA): https://gdex.ucar.edu/datasets/d337000/ (last access: 10 May 2026; National Centers For Environmental Prediction/National Weather Service/NOAA/U.S. Department Of Commerce, 2008) and https://gdex.ucar.edu/datasets/d735000/ (last access: 10 May 2026; National Centers For Environmental Prediction/National Weather Service/NOAA/U.S. Department Of Commerce, 2009). ECMWF deterministic and ensemble analyses were provided by the Centre for Climate Research Singapore (CCRS) and are available from the corresponding author upon request.

Author contributions

X.Z., Z.L. and L.J. developed the methods. X.Z. conducted the experiments, performed the testing and validation, and prepared the manuscript. X.Z. and L.J. contributed to additional testing and validation of the datasets and results. Z.L. provided valuable feedback on the development and implementation of the data assimilation procedures, as well as on the manuscript. T.S., I.-H.C., D.B., and J.M. provided technical assistance and offered scientific suggestions that helped improve the study. All authors have read and agreed to the published version of the manuscript.

Competing interests

The contact author has declared that none of the authors has any competing interests.

Disclaimer

Acknowledgements

The authors gratefully acknowledge the SINGV-NG(MPAS) team from both the NSF National Center for Atmospheric Research and the Centre for Climate Research Singapore (CCRS) for their dedicated collaboration in the development of the system. We also acknowledge the Computational and Information Systems Laboratory (CISL) at NSF National Center for Atmospheric Research (NCAR) for their technical support.

Financial support

This work was supported by the Centre for Climate Research Singapore (CCRS) of the Meteorological Service Singapore.

References

Bannister, R. N.: A review of operational methods of variational and ensemble-variational data assimilation, *Q. J. R. Meteorol. Soc.*, 143, 607–633, https://doi.org/10.1002/qj.2982, 2017.

Barker, D., Huang, X.-Y., Liu, Z., Auligné, T., Zhang, X., Rugg, S., Ajjaji, R., Bourgeois, A., Bray, J., Chen, Y., Demirtas, M., Guo, Y.-R., Henderson, T., Huang, W., Lin, H.-C., Michalakes, J., Rizvi, S., and Zhang, X.: The Weather Research and Forecasting Model's Community Variational/Ensemble Data Assimilation System: WRFDA, *Bull. Amer. Meteor. Soc.*, 93, 831–843, https://doi.org/10.1175/BAMS-D-11-00167.1, 2012.

Bessho, K., Date, K., Hayashi, M., Ikeda, A., Imai, T., Inoue, H., Kumagai, Y., Miyakawa, T., Murata, H., Ohno, T., Okuyama, A., Oyama, R., Sasaki, Y., Shimazu, Y., Shimoji, K., Sumida, Y., Suzuki, M., Taniguchi, H., Tsuchiyama, H., Uesawa, D., Yokota, H., and Yoshida, R.: An introduction to Himawari-8/9—Japan's new-generation geostationary meteorological satellites, *J. Meteorol. Soc. Jpn.*, 94, 151–183, https://doi.org/10.2151/jmsj.2016-009, 2016.

Chan, M.-Y., Zhang, F., Chen, X., and Leung, L. R.: Potential Impacts of Assimilating All-Sky Satellite Infrared Radiances on Convection-Permitting Analysis and Prediction of Tropical Convection, *Mon. Weather Rev.*, 148, 3203 – 3224, https://doi.org/10.1175/MWR-D-19-0343.1, 2020.

Chen, I.-H., Patel, P., Furtado, K., Wang, W., Liu, Z., Barker, D., Dudhia, J., and Zhang, H.: Performance evaluation of regional weather predictions with the Model for Prediction Across Scales–Atmosphere (MPAS-A) over the Maritime Continent, *Q. J. R. Meteorol. Soc.*, e70129, https://doi.org/10.1002/qj.70129, 2026.

Degelia, S. K., Wang, X., Wang, Y., and Johnson, A.: Assimilation of GOES-16 ABI All-Sky Radiance Observations in RRFS Using EnVar: Methodology, System Development, and Impacts for a Severe Convective Event, *Mon. Weather Rev.*, 151, 2739–2758, https://doi.org/10.1175/MWR-D-23-0057.1, 2023.

Done, J. M., Davis, C. A., and Weisman, M. L.: The next generation of NWP: Explicit forecasts of convection using the Weather Research and Forecasting (WRF) model, *Atmos. Sci. Lett.*, 5, 110–117, https://doi.org/10.1002/asl.72, 2004.

Duda, M., Jacobsen, D., Petersen, M., Hoffman, M., ldfowler58, Turner, A. K., Asay-Davis, X., Ringler, T., Roekel, L. V., Curry, M., Lipscomb, W., stephenprice, skamaroc, Jeffery, N., Heinzeller, D., Woodring, J., Wolfram, P. J., Dickerson, G. D., maltrud, Saenz, J. Nick, weiwangncar, Mametjanov, A., mperego, Werner, K., Wolfe, J., W, J., Jones, P., Werner, K., and Larofeticus: MPAS-Dev/MPAS-Model: MPAS Version 8.2.2 (v8.2.2), Zenodo [code], https://doi.org/10.5281/zenodo.13821326, 2024.

Ek, M. B., Mitchell, K. E., Lin, Y., Rogers, E., Grunmann, P., Koren, V., Gayno, G., and Tarpley, J. D.: Implementation of Noah land surface model advances in the National Centers for Environmental Prediction operational mesoscale Eta model, *J. Geophys. Res. Atmos.*, 108, 8851, https://doi.org/10.1029/2002JD003296, 2003.

Feng, C. and Pu, Z.: All-Sky Assimilation of GOES-16 Water Vapor Channels in Consideration of Cloud-Dependent Interchannel Observation-Error Correlations, *Mon. Weather Rev.*, 153, 23–47, https://doi.org/10.1175/MWR-D-24-0038.1, 2025.

Gao, J., Heinselman, P. L., Xue, M., Wicker, L. J., Yussouf, N., Stensrud, D. J., and Droegemeier, K. K.: The Numerical Prediction of Severe Convective Storms: Advances in Research and Applications, Remaining Challenges, and Outlook for the Future, *Encyclopedia of Atmospheric Sciences*, 372–393, https://doi.org/10.1016/B978-0-323-96026-7.00127-2, 2026.

Geer, A. J., Migliorini, S., and Matricardi, M.: All-sky assimilation of infrared radiances sensitive to mid- and upper-tropospheric moisture and cloud, *Atmos. Meas. Tech.*, 12, 4903–4929, https://doi.org/10.5194/amt-12-4903-2019, 2019.

Gehne, M., Wolding, B., Dias, J., and Kiladis, G. N.: Diagnostics of tropical variability for numerical weather forecasts, *Wea. Forecasting*, 37, 1661–1680, https://doi.org/10.1175/WAF-D-21-0204.1, 2022.

Grell, G. A. and Freitas, S. R.: A scale and aerosol aware stochastic convective parameterization for weather and air quality modeling, *Atmos. Chem. Phys.*, 14, 5233–5250, https://doi.org/10.5194/acp-14-5233-2014, 2014.

Guerrette, J. J., Liu, Z., Snyder, C., Jung, B.-J., Schwartz, C. S., Ban, J., Vahl, S., Wu, Y., Baños, I. H., Yu, Y. G., Ha, S., Trémolet, Y., Auligné, T., Gas, C., Ménétrier, B., Shlyaeva, A., Miesch, M., Herbener, S., Liu, E., Holdaway, D., and Johnson, B. T.: Data assimilation for the Model for Prediction Across Scales – Atmosphere with the Joint Effort for Data assimilation Integration (JEDI-MPAS 2.0.0-beta): ensemble of 3D ensemble-variational (En-3DEnVar) assimilations, *Geosci. Model Dev.*, 16, 7123–7142, https://doi.org/10.5194/gmd-16-7123-2023, 2023.

Harnisch, F., Weissmann, M., and Periáñez, A.: Error model for the assimilation of cloud-affected infrared satellite observations in an ensemble data assimilation system, *Q. J. R. Meteorol. Soc.*, 142, 1797 – 1808, https://doi.org/10.1002/qj.2776, 2016.

Honda, T., Kotsuki, S., Lien, G.-Y., Maejima, Y., Okamoto, K., and Miyoshi, T.: Assimilation of Himawari-8 all-sky radiances every 10 minutes: Impact on precipitation and flood risk prediction, *J. Geophys. Res. Atmos.*, 123, 965 – 976, https://doi.org/10.1002/2017JD027096, 2018.

Hong, S.-Y., and Lim, J.-O. J.: The WRF single-moment 6-class microphysics scheme (WSM6), *J. Korean Meteor. Soc.*, 42, 129–151, https://www2.mmm.ucar.edu/wrf/users/workshops/WS2006/abstracts/PSession05/P5_4_Hong.pdf, 2006.

Hu, G., Dance, S. L., Bannister, R. N., Chipilski, H. G., Guillet, O., Macpherson, B., Weissmann, M., and Yussouf, N.: Progress, challenges, and future steps in data assimilation for convection-permitting numerical weather prediction: Report on the virtual meeting held on 10 and 12 November 2021, *Atmos. Sci. Lett.*, 24, e1130, https://doi.org/10.1002/asl.1130, 2023.

Hu, X.-M., Klein, P. M., and Xue, M.: Evaluation of the updated YSU planetary boundary layer scheme within WRF for wind resource and air quality assessments, *J. Geophys. Res. Atmos.*, 118, 10490–10505, https://doi.org/10.1002/jgrd.50823, 2013.

Hutt, A., Schraff, C., Anlauf, H., Bach, L., Baldauf, M., Bauernschubert, E., Cress, A., Faulwetter, R., Fundel, F., Köpken-Watts, C., Reich, H., Schomburg, A., Schröttle, J., Stephan, K., Stiller, O., Weissmann, M., and Potthast, R.: Assimilation of SEVIRI water vapor channels with an ensemble Kalman filter on the convective scale, *Front. Earth Sci.*, 8, 70, https://doi.org/10.3389/feart.2020.00070, 2020.

Iacono, M. J., Delamere, J. S., Mlawer, E. J., Shephard, M. W., Clough, S. A., and Collins, W. D.: Radiative forcing by long-lived greenhouse gases: Calculations with the AER radiative transfer models, *J. Geophys. Res. Atmos.*, 113, D13103, https://doi.org/10.1029/2008JD009944, 2008.

Japan Meteorological Agency: JMA Himawari-8/9 data, distributed via the NOAA Himawari Open Data service, Registry of Open Data on AWS [data set], https://registry.opendata.aws/noaa-himawari/, last access: 10 May 2026, 2026.

Japan Aerospace Exploration Agency: JAXA Himawari Monitor/P-Tree System, Japan Aerospace Exploration Agency [data set], https://www.eorc.jaxa.jp/ptree/index.html, last access: 10 May 2026, 2026.

Johnson, A. and Wang, X.: Impacts of Initial Condition Perturbation Blending in 10- and 40-Member Convection-Allowing Ensemble Forecasts, *Mon. Weather Rev.*, 152, 1421–1441, https://doi.org/10.1175/MWR-D-23-0188.1, 2024.

Johnson, B. T., Dang, C., Stegmann, P., Liu, Q., Moradi, I., and Auligné, T.: The Community Radiative Transfer Model (CRTM): Community-Focused Collaborative Model Development Accelerating Research to Operations, *Bull. Amer. Meteor. Soc.*, 104, E1817–E1830, https://doi.org/10.1175/BAMS-D-22-0015.1, 2023.

Johnson, B. T., Dang, C., Rosinski, J., YingtaoMa, StegmannJCSDA and Kasprzyk, P.:JCSDA/crtm: v2.4.1-jedi public release for UFO/JEDI (v2.4.1-jedi), Zenodo [code], https://doi.org/10.5281/zenodo.7823722, 2023.

Joint Center for Satellite Data Assimilation and National Center for Atmospheric Research: JEDI-MPAS Data Assimilation System v3.0.3 (3.0.3), Zenodo [code], https://doi.org/10.5281/zenodo.19209009, 2025.

Jones, T. A., Skinner, P., Yussouf, N., Knopfmeier, K., Reinhart, A., Wang, X., Bedka, K., Smith Jr., W., and Palikonda, R.: Assimilation of GOES-16 radiances and retrievals into the Warn-on-Forecast System, *Mon. Weather Rev.*, 148, 1829–1859, https://doi.org/10.1175/MWR-D-19-0379.1, 2020.

Jung, B.-J., Ménétrier, B., Snyder, C., Liu, Z., Guerrette, J. J., Ban, J., Baños, I. H., Yu, Y. G., and Skamarock, W. C.: Three-dimensional variational assimilation with a multivariate background error covariance for the Model for Prediction Across Scales – Atmosphere with the Joint Effort for Data assimilation Integration (JEDI-MPAS 2.0.0-beta), *Geosci. Model Dev.*, 17, 3879–3895, https://doi.org/10.5194/gmd-17-3879-2024, 2024.

Kugler, L. and Weissmann, M.: The synergy of assimilating visible and infrared radiances and radar observations, *Q. J. R. Meteorol. Soc.*, 151, e4938, https://doi.org/10.1002/qj.4938, 2025.

Li, J., Geer, A. J., Okamoto, K., Otkin, J. A., Liu, Z., Han, W., and Wang, P.: Satellite all-sky infrared radiance assimilation: Recent progress and future perspectives, *Adv. Atmos. Sci.*, 39, 9–21, https://doi.org/10.1007/s00376-021-1088-9, 2022.

Liu, Z., Snyder, C., Guerrette, J. J., Jung, B.-J., Ban, J., Vahl, S., Wu, Y., Trémolet, Y., Auligné, T., Ménétrier, B., Shlyaeva, A., Herbener, S., Liu, E., Holdaway, D., and Johnson, B. T.: Data assimilation for the Model for Prediction Across Scales – Atmosphere with the Joint Effort for Data assimilation Integration (JEDI-MPAS 1.0.0): EnVar implementation and evaluation, *Geosci. Model Dev.*, 15, 7859–7878, https://doi.org/10.5194/gmd-15-7859-2022, 2022.

Matsunobu, T., Puh, M., and Keil, C.: Flow- and scale-dependent spatial predictability of convective precipitation combining different model uncertainty representations, *Q. J. R. Meteorol. Soc.*, 150, 2364–2381, https://doi.org/10.1002/qj.4713, 2024.

Medeiros, B., Clement, A. C., Benedict, J. J., and Coauthors: Investigating the impact of cloud-radiative feedbacks on tropical precipitation extremes, *npj Clim. Atmos. Sci.*, 4, 18, https://doi.org/10.1038/s41612-021-00174-x, 2021.

Nakanishi, M. and Niino, H.: An Improved Mellor – Yamada Level-3 Model with Condensation Physics: Its Design and Verification, *Bound.-Lay. Meteorol.*, 112, 1–31, https://doi.org/10.1023/B:BOUN.0000020164.04146.98, 2004.

Nakanishi, M. and Niino, H.: Development of an Improved Turbulence Closure Model for the Atmospheric Boundary Layer, *J. Meteorol. Soc. Jpn.*, 87, 895–912, https://doi.org/10.2151/jmsj.87.895, 2009.

National Centers for Environmental Prediction/National Weather Service/NOAA/U.S. Department of Commerce: NCEP ADP Global Upper Air and Surface Weather Observations (PREPBUFR format), Research Data Archive at the National Center for Atmospheric Research, Computational and Information Systems Laboratory [data set], https://gdex.ucar.edu/datasets/d337000/, 2008.

National Centers for Environmental Prediction/National Weather Service/NOAA/U.S. Department of Commerce: NCEP GDAS Satellite Data 2004 – continuing, Research Data Archive at the National Center for Atmospheric Research, Computational and Information Systems Laboratory [data set], https://gdex.ucar.edu/datasets/d735000/, 2009.

Nystrom, R. G., Snyder, C., Liu, Z., Jung, B.-J., Ban, J., and Baños, I. H.: A hybrid four-dimensional variational data assimilation system for the Model for Prediction Across Scales (MPAS-atmosphere): Leveraging the Joint Effort for Data assimilation Integration (JEDI), *J. Adv. Model. Earth Syst.*, 17, e2025MS005183, https://doi.org/10.1029/2025MS005183, 2025.

Rao, X., Zhu, K., Zhao, K., Chen, X., Hu, S., Liu, X., and Zhou, A.: Evaluation and Error Source Analysis of Convection-Permitting Forecasts for Localized Nocturnal Rainfall Over a Complex Mountainous Region in Pearl River Delta, South China, *J. Geophys. Res. Atmos.*, 128, e2023JD039065, https://doi.org/10.1029/2023JD039065, 2023.

Rendon, J. and Zhang, Y.: Impact of microphysical parameterizations on satellite all-sky infrared data assimilation and practical predictability of Hurricane Harvey (2017)., *J. Geophys. Res. Atmos.*, 130, e2024JD042697, https://doi.org/10.1029/2024JD042697, 2025.

Roberts, N. M. and Lean, H. W.: Verification of Rainfall Accumulations from High-Resolution Forecasts of Convective Events., *Mon. Weather Rev.*, 136, 78–97, https://doi.org/10.1175/2007MWR2123.1, 2008.

Ruppert, J. H. and Chen, X.: Island rainfall enhancement in the maritime continent, *Geophys. Res. Lett.*, 47, e2019GL086545, https://doi.org/10.1029/2019GL086545, 2020.

Sawada, Y., Okamoto, K., Kunii, M., and Miyoshi, T.: Assimilating every-10-minute Himawari-8 infrared radiances to improve convective predictability, *J. Geophys. Res. Atmos.*, 124, 2546 – 2561, https://doi.org/10.1029/2018JD029643, 2019.

Scheck, L., Weissmann, M., and Bach, L.: Assimilating visible satellite images for convective-scale numerical weather prediction: A case-study, *Q. J. R. Meteorol. Soc.*, 146, 3165–3186, https://doi.org/10.1002/qj.3840, 2020.

Skamarock, W. C., Klemp, J. B., Duda, M. G., Fowler, L. D., Park, S.-H., and Ringler, T. D.: A Multiscale Nonhydrostatic Atmospheric Model Using Centroidal Voronoi Tesselations and C-Grid Staggering, *Mon. Weather Rev.*, 140, 3090–3105, https://doi.org/10.1175/MWR-D-11-00215.1, 2012.

Skamarock, W. C., Duda, M. G., Ha, S., and Park, S.-H.: Limited-Area Atmospheric Modeling Using an Unstructured Mesh, *Mon. Weather Rev.*, 146, 3445–3460, https://doi.org/10.1175/MWR-D-18-0155.1, 2018.

Stengel, M., Lindskog, M., Undén, P., and Gustafsson, N.: The impact of cloud-affected IR radiances on forecast accuracy of a limited-area NWP model, *Q. J. R. Meteorol. Soc.*, 139, 2081–2096, https://doi.org/10.1002/qj.2102, 2013.

Stephens, G. L., Shiro, K. A., Hakuba, M. Z., and Coauthors: Tropical deep convection, cloud feedbacks and climate sensitivity, *Surv. Geophys.*, 45, 1903–1931, https://doi.org/10.1007/s10712-024-09831-1, 2024.

Trémolet, Y. and Auligné, T.: The Joint Effort for Data Assimilation Integration (JEDI), *JCSDA Q. Newslett.*, 66, 1 – 5, https://doi.org/10.25923/RB19-0Q26, 2020.

Wang, Y., Chen, M., Min, J., Zhang, F., and Liu, Z.: Improving the prediction of heavy rainfall with rapid-update dual-resolution hybrid En3DVar assimilation of all-sky AHI infrared water vapor radiances, *Atmos. Res.*, 280, 106429, https://doi.org/10.1016/j.atmosres.2022.106429, 2022.

Xu, D., Zhang, X., Liu, Z., and Shen, F.: All-sky infrared radiance data assimilation of FY-4A AGRI with different physical parameterizations for the prediction of an extremely heavy rainfall event, *Atmos. Res.*, 293, 106898, https://doi.org/10.1016/j.atmosres.2023.106898, 2023.

Xu, K.-M., and Randall, D. A.: A semiempirical cloudiness parameterization for use in climate models, *J. Atmos. Sci.*, 53, 3084–3102, https://doi.org/10.1175/1520-0469(1996)053<3084:ASCPFU>2.0.CO;2, 1996.

Xu, L., Cheng, W., Deng, Z., Liu, J., Wang, B., and Lu, B.: Assimilation of the FY-4A AGRI Clear-Sky Radiance Data in a Regional Numerical Model and Its Impact on the Forecast of the “21·7” Henan Extremely Persistent Heavy Rainfall, *Adv. Atmos. Sci.*, 40, 920–936, https://doi.org/10.1007/s00376-022-1380-3, 2023.

Xie, Y., Weng, F., Ye, C., Liu, R., and Han, X.: All-sky assimilation of FY-4B AGRI reflectance in the CMA-MESO model with ARMS as a forward operator, *J. Geophys. Res. Atmos.*, 130, e2025JD043600, https://doi.org/10.1029/2025JD043600, 2025.

Yang, J., Pu, Z., Zhang, L., and Zhang, S.: Assimilation of GOES imager clear-sky radiances in a convection-permitting WRF model for short-range forecasting, *Mon. Weather Rev.*, 145, 3129–3147, https://doi.org/10.1175/MWR-D-16-0393.1, 2017.

Zhang, X., Xu, D., Shen, F., and Min, J.: Impacts of offline nonlinear bias correction schemes using the machine learning technology on the all-sky assimilation of cloud-affected infrared radiances, *J. Adv. Model. Earth Syst.*, 16, e2024MS004281, https://doi.org/10.1029/2024MS004281, 2024.

Zhang, F., Minamide, M., and Clothiaux, E. E.: Potential impacts of assimilating all-sky infrared satellite radiances from GOES-R on convection-permitting analysis and prediction of tropical cyclones, *Geophys. Res. Lett.*, 43, 2954–2963, https://doi.org/10.1002/2016GL068468, 2016.

Zhu, L., Xue, M., Kong, R., and Min, J.: Direct assimilation of all-sky GOES-R ABI radiances in GSI EnKF for the analysis and forecasting of a mesoscale convective system, *Mon. Weather Rev.*, 151, 737–760, https://doi.org/10.1175/MWR-D-21-0293.1, 2023.

Zou, X., Qin, Z., and Zheng, Y.: Improved tropical storm forecasts with GOES-13/15 imager radiance assimilation and asymmetric vortex initialization in HWRF, *Mon. Weather Rev.*, 143, 2485–2505, https://doi.org/10.1175/MWR-D-14-00223.1, 2015.